POLITECNICO
MILANO 1863

SCUOLA DI INGEGNERIA INDUSTRIALE
E DELL'INFORMAZIONE

Relative motion control of cluster formation in a geostationary orbit with the J_{22} perturbation

Tesi di Laurea Magistrale in
Space Engineering - Ingegneria Spaziale

Author: **Luca Rizzieri**

Student ID: 945691
Advisor: Prof. Camilla Colombo
Co-advisors: Francesca Scala
Academic Year: 2020-21

A chi avrebbe voluto essere qui
ed è comunque presente

When referring to this work, full bibliographic details must be given:

Rizzieri Luca, "Relative motion control of cluster formation in a geosynchronous orbit with the J_{22} perturbation". 2022, Politecnico di Milano, Faculty of Industrial Engineering, Master in Space Engineering, Supervisor: Camilla Colombo, Co-supervisor: Francesca Scala.

Printed in Italy.

Abstract

Formation flying reaches out to the latest demands of the up-to-date space industry. It allows meeting the urge for sustainability, both economically, reducing the costs, and environmentally, providing tools for monitoring and removing space debris. The constant cut of volumes and masses, due to the technology miniaturisation process, opens up to new applications in different fields: from communication to Earth observation. That is why, in the present day, satellite constellations are a crucial topic in the space debate.

In particular, remote sensing missions can particularly benefit from formation of satellites bringing a distributed payload. By forming a specific geometry and by keeping it tight, a higher aperture can be obtained. In this way, it is possible to enhance the spatial resolution needed for scientific imaging without using a massive spacecraft. One of the latest development consists of multi-satellite passive microwave interferometric radiometry. Synthetic Aperture Radiometry allows obtaining excellent results in Earth Observation. Further development is to increase the time resolution and the only way is by increasing orbit altitude. For example, exploiting geostationary orbit.

The ensemble of all these characteristics outlines the limits of the case studied in this Thesis: a remote sensing mission of satellites flying in formation in a geosynchronous equatorial orbit. A multi-satellite configuration will grant the requirements needed for scientific instrumentation in terms of resolution. The presented work provides precise modelling of the relative motion control. A new State Transition Matrix is introduced to include the effect due to the non-spherically symmetry of Earth's mass distribution up to J_{22} in an analytical model. The accounted perturbation acts on the satellites making their orbit and consequently the formation change. On one hand, the relative position has to be kept as rigid as possible for granting the spatial resolution of the imaging system, at the same time the satellites must remain in their longitudinal slot.

Employing the mean Relative Orbital Elements, the system dynamics can be linearised. This allows the design and verification of autonomous relative guidance navigation based on Linear Quadratic Regulators. The implemented control algorithm, using continuous feedback, effectively achieves the performance required by satellite constellation maintenance. Cold gas and electric thrusters are eligible to perform the control action needed.

The objective of this research is to analyse a remote sensing mission in a geostationary orbit exploiting a distributed payload. The dynamic model aims at matching the accuracy of the high-fidelity simulation and due to State Transition Matrix, well known for its computational efficiency, the hardware effort is reduced. The closed-loop control provides the centimetres to meters accuracy expected for this mission. The simulation carried out shows how optimal low-thrust control minimises the formation-keeping Δv. Finally, the present work opens up to future studies aiming at implementing this technology on a real mission. For instance, the perturbations due to third bodies can be taken into account superposing the effects. Moreover, an investigation on satellites' attitude for power budget purposes can be implemented.

This thesis is part of the COMPASS project: "Control for orbit manoeuvring by surfing through orbit perturbations" (Grant agreement No 679086).
This project is European Research Council (ERC) funded project under the European Union's Horizon 2020 research (www.compass.polimi.it).

Keywords: Formation flying, Earth Observation, low thrust control, GEO, Relative dynamics

Sommario

Il volo in formazione va incontro alle ultime necessità dell'industria dello spazio del giorno d'oggi. Permette di soddisfare la corsa alla sostenibilità, tanto economica come ambientale. Il continuo taglio ai volumi e alle masse, dovuto al continuo processo di miniaturizzazione, apre a nuove applicazioni in diversi campi: dalla comunicazione all'osservazione terrestre. Questo è il motivo per cui attualmente le costellazioni di satelliti sono al centro del dibattito della comunità dello spazio.

In particolare, missioni di telerilevamento possono particolarmente trarre vantaggio da formazioni di satelliti che trasportano un carico pagante distribuito. Formando geometrie specifiche e mantenendole rigide, si possono ottenere aperture maggiori. In questo modo, è possibile migliorare la risoluzione spaziale di cui la strumentazione ha bisogno, senza utilizzare satelliti di grandi dimensioni. Uno degli ultimi sviluppi consiste nella radiometria con microonde sfruttando l'interferometria tra più satelliti. La cosiddetta Radiometria ad Apertura Sintetica permette di ottenere risultati eccellenti per l'osservazione della Terra. Lo sviluppo futuro è legato all'aumento della risoluzione temporale e questo può solo essere ottenuto aumentando l'altitudine dell'orbita. Per esempio in orbita Geostazionaria.

L'insieme di tutte queste caratteristiche, delinea i confini del caso studiato in questa Tesi: una missione di telerilevamento di satelliti che volano in formazione in un orbita equatoriale Geosincrona. Una configurazione con più satelliti assicurerà il rispetto dei requisiti necessari alla strumentazione scientifica in termini di risoluzione. Il lavoro qui presentato fornisce una modellizzazione precisa del controllo del movimento relativo. Una nuova Matrice di Transizione dello Stato viene introdotta per includere l'effetto dovuto alla non simmetria sferica della distribuzione della massa terrestre, fino a J_{22}, in un modello analitico. La perturbazione presa in esame agisce sui satelliti facendo cambiare la loro orbita e la formazione stessa. Da una parte, la posizione relativa deve essere mantenuta più fissa possibile per garantire la risoluzione delle immagini, dall'altra i satelliti devono rimanere nel loro slot longitudinale.

Per mezzo degli elementi relativi medi, la dinamica del sistema può essere linearizzata. Questo permette di progettare e verificare un controllo relativo autonomo della navigazione basato su Regolatori Lineari Quadratici. L'algoritmo di controllo implementato, utilizzando una retroazione continua, raggiunge efficacemente le prestazioni richieste dal mantenimento della costellazione di satelliti. Attuatori elettrici e a gas freddi sono selezionabili per sviluppare l'azione di controllo necessaria.

L'obiettivo di questa ricerca è quello di analizzare una missione di telerilevamento in orbita Geostazionaria sfruttando un carico pagante distribuito. Il modello dinamico punta ad eguagliare l'accuratezza dei simulatori ad alta fedeltà e grazie alla Matrice di Transizione dello Stato, nota per la sua efficienza computazionale, ridurre lo sforzo di hardware. Il controllo ad anello assicura l'accuratezza dell'ordine dai centimetri ai metri prevista per questo tipo di missione. La simulazione ottenuta mostra come il controllo ottimo a spinta bassa minimizza il Δv dovuto al mantenimento della formazione. Infine, il lavoro presentato apre la strada a futuri studi concentrati a rendere questa tecnologia valida per una vera missione. Per esempio, altre perturbazioni dovute a terzi corpi possono essere prese in considerazione ed aggiunte al modello super-ponendo gli effetti. Inoltre, un'analisi sull'orientamento dei satelliti può essere aggiunto ai fini della gestione del bilancio di potenza.

Questa tesi è parte del progetto COMPASS: "Control for orbit manoeuvring by surfing through orbit perturbation" (Sovvenzione No 679086).
Questo progetto è finanziato dal Consiglio Europeo della Ricerca (ERC) nell'ambito della ricerca dell'Unione Europea Horizon 2020 (www.compass.polimi.it).

Parole chiave: Volo in Formazione, Osservazione della Terra, Controllo con bassa spinta, GEO, Dinamica Relativa

Contents

List of Figures

List of Tables

1 | Introduction

At the time being, systems such as Global Positioning System (GPS) or Galileo, are part of everyday life. These services have brought numerous benefits to any day to day activity and now are taken for granted. Their implementation has been the first example of satellites flying in a designed formation working together for a shared goal [1]. This has marked the beginning of Satellites Constellations and Formation Flight (FF).

Over the years, different fields have exploited multiple satellites operating in formation, to benefit from the promising outcomes arising [2]. Unavoidably, each application requires specific solutions that, in their turn, lead to new implementations. For example, navigation and communication purposes use constellation formations of satellites, while trailing or cluster formations are more often adopted for remote sensing. In the first configuration, satellites are deployed to reach the optimal ground coverage. On the other hand, a completely different logic is behind trailing formation. In this case, the satellites are released on the same orbit chasing each other. Used mainly for meteorological and environmental purposes, the interval between two passages on the same path gives back an evolution in time [3]. Finally, cluster formations are tight configurations of many satellites that allow performing high-resolution interferometry even in space.

With the advent of CubeSats, made possible by the progressive miniaturisation of most components needed, the development timescales are reduced, the launch logistics became easier and the costs associated less expensive. These factors allow the implementation of distributed payload missions. Missions based on larger satellites are now more and more replaced by multiple satellites configurations providing the same services. Moreover, the unstoppable evolution of technology opens up new opportunities for exploiting formation flying and for some upcoming problems it can be seen as part of the solution.

This does not mean that single large spacecraft will be abandoned. Currently, the James Webb Space Telescope (JWST) has reached the Lagrange equilibrium point L_2 and it is performing calibration of its instrumentation. With its 6.6 m diameter mirror, JWST is the biggest ever launched and aims to observe far beyond the possibility of its predecessor: Hubble Space Telescope (HST) [4]. But clusters of micro- or nano-spacecraft have another

target: enabling capabilities in terms of time and spatial resolution that would not be achievable by single large spacecraft. The potentially huge impact of the latter cited technology on Earth and Space observation is the reason for the extensive effort in research on this field, in which this work would like to give a small contribution.

The aim of the Thesis, presented from here on, is to enhance the precise relative motion in a Geosynchronous Earth Orbit (GEO). First, the dynamics of the satellite is developed, taking into account Geodetic effects. Earth gravitational field, model as a potential, up to J_{22} perturbation. Then, implementing an effective control to comply with the requirements imposed by the scientific payload.

1.1. Economic considerations

The GEO is a special case of the Geosynchronous Orbits (GSO). The main feature is that the orbit period of the satellite matches exactly the sidereal day. In other words, the spacecraft completes a revolution around the Earth at the same time as Earth's rotation on its axis. By definition, a GSO lays on the equatorial axis and the peculiarity of the GEO is to be a circular GSO. If not perturbed, the ground track of that satellite is a point, which means that for an observer on Earth's surface the position in the sky remains the same. This characteristic is extremely crucial, most of all for communication purposes.

Nowadays, due to GEO advantages, more than 570 satellites are listed in that orbit. As of January 2022, according to UCS Satellite Database [5]. All those spacecraft are spread along the equator line at different longitudes from East to West. The traffic in this zone is regulated. Longitudinal slots constrain each spacecraft and station-keeping is performed to allow the satellite to stay in the slot without being driven out by perturbations. Nevertheless, the space is not "infinite", at least in that region. Consequently, to maximise the effective use of a certain longitudinal position, some concepts include multiple satellites accommodation in the same slot. The resulting benefits are exploited in different fields: from telecommunications to weather and from navigation to remote sensing.

Performing Earth or deep space observation from GEO orbit is extremely demanding. Autonomous inter-satellite control and collision avoidance functions will be needed. On the other hand, a fleet of smaller spacecraft can provide a communication network that can be tailored for different demands. Spacecraft formation flying has been proposed for various applications such as optical interferometry for imaging. Moreover, massive communications satellites can be used as a Chief in a cluster formation. Potentially, the overall cost of a GEO mission can also be reduced. Sharing the same longitudinal slot (and therefore the same frequency for communication) can decrease the leasing fee.

1.2. State of the art

Both the fields of precision satellite formation flight and interferometric microwave radiometry are undergoing rapid growth. This section presents some of the key missions and future concepts representing the current state of the art.

Magnetospheric Multi-scale (MMS) is a NASA mission, launched in 2015, to study how the Sun's and Earth's magnetic fields connect and disconnect. On the heels of ESA **Cluster II** mission investigating the Earth's magnetic field in the early 2000s, this mission falls in the space weather research area. This phenomenon affects modern technological systems such as telecommunications networks, GPS navigation, and electrical power grids. An adjustable pyramid-like formation of 4 identically instrumented spacecraft enables the three-dimensional observation of plasma, fields and particles in a near-equatorial orbit. This mission has proven that high resolution, both spatial and temporal, is achievable by maintaining a regular tetrahedral formation [6].

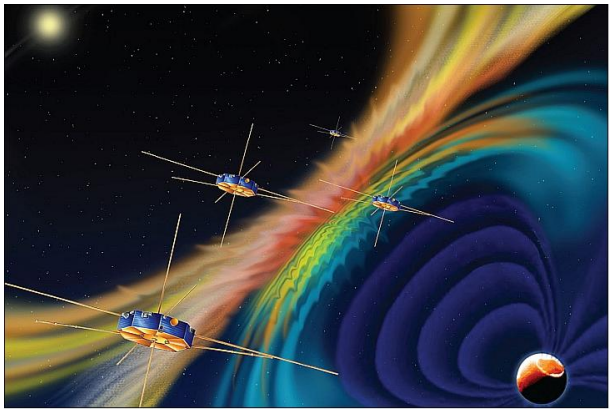

Figure 1.1: **MMS** formation as a science instrument concept [7].

Project for On-Board Autonomy (PROBA-3) is the latest spacecraft in the program. With this mission, the ESA aims at demonstrating the technologies required for the formation flying of multiple spacecraft in the fields of space science, Earth Observation and surveillance. The concept includes 2 spacecraft, released in Highly-elliptical Earth Orbit (HEO), close to one another flying in formation with accurate control of the relative position. Moreover, with the launch planned for 2023, this mission will validate new techniques and technologies developed for relative motion throughout a series of precise manoeuvres. At the same time, after proving that the Technology Readiness level is at its latest step (TRL-9), this constellation will contribute to the improvement of the required tools, such as simulators. The tight formation, spaced about 100 m, will incorporate a 6-DOF control with an accuracy on the relative position of less than 1 mm [8].

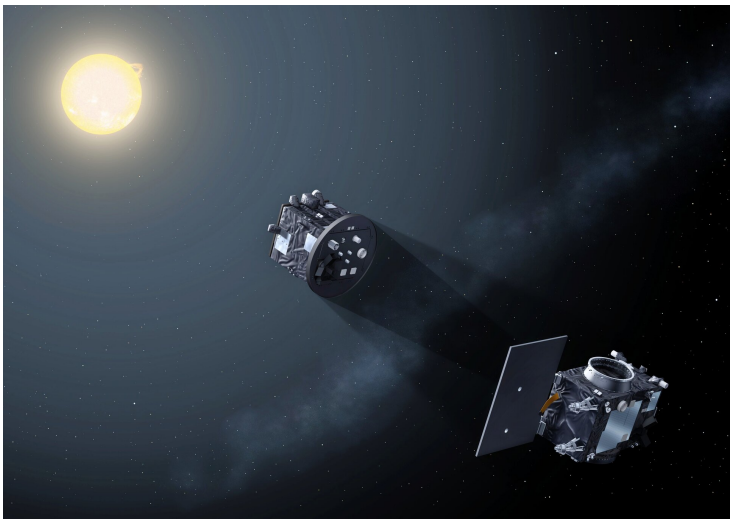

Figure 1.2: **PROBA-3**'s pair of satellites [9].

Moreover, a scientific payload will be flown. Studies about Sun composition will be carried out. Exploiting the spacecraft's position, one of them will exactly cover the solar disc from the coronagraph spacecraft's instrument vision. In this way, Sun's corona can be observed with unprecedented clarity.

HelioSwarm is a NASA MidEx mission comprised of 9 spacecraft selected for launch in 2028. Designed to study the plasma and magnetic fields that compose solar wind and its effect on the solar system and the universe. It represents a new step for multi-satellite missions, a cluster formation made up of one Chief and eight Deputies satellites, to measure at multiple scales simultaneously [10]. The flight dynamics of the nine spacecraft requires onboard propulsion that grants the ideal inter-spacecraft separation. The optimal geometry to enable the application is established by analysing different models accounting for turbulence due to the lunar resonant Earth orbit.

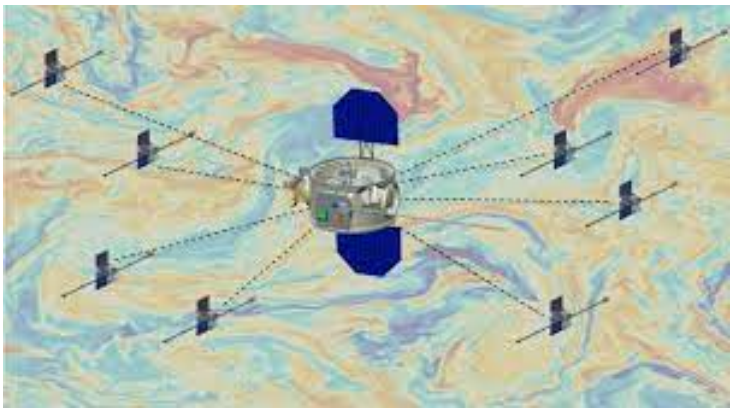

Figure 1.3: **HelioSwarm** cluster formation [11].

All these missions require a precise formulation for the relative dynamics of multi-satellite formations. The main field of research is the implementation of a model which could better represent the environment, especially for Low Earth Orbit (LEO). The main perturbations to be modelled at low altitudes are the Earth's oblateness and the drag. To accomplish the task several configurations have been proposed, starting from the set of coordinates. In [12], the authors utilise Cartesian coordinates for developing a second-order model for the relative dynamics perturbed by J_2. Using the same frame, a linear model has also been implemented in [13]. Another approach is the one followed in [14], this time the selected set is composed by the Relative orbital Elements (ROE) and the model accounts for drag and Earth's non-spherical symmetry mass distribution. Also, this latter is a linear model. The effects of non-conservative forces are embedded in a formulation composed of linear equations to allow autonomous relative motion determination and control.

After the aforementioned overview of existing formation flying missions, it is also worth taking a look at the technology required for remote sensing in GEO. Geostationary altitude needs a larger aperture to achieve the same resolution reached in LEO. At the same time, costs and volume management drives the design in the opposite direction. A Synthetic Aperture Radiometers (SAR), exploiting interferometry, utilises a set of smaller antenna to synthesise a larger one. This technique has already been validated in space. The LEO NASA mission **Soil Moisture and Ocean Salinity (SMOS)** was a success [15]. Further development, following on from what learned, was the application in GEO.

Geostationary Atmospheric Sounder (GAS) is the ESA sounder concept for meteorology purposes [16]. Laying in a Geostationary orbit, it aims at predicting the evolution of atmospheric temperature and water vapour for phenomena forecast. Composed of a single satellite with a Y-shaped array, this spacecraft will host a microwave instrument for radiometry. The spatial resolution required is about 30 km and the time interval between two different images is about 15 minutes. Given the distance of geostationary orbit, to obtain that precision, the large aperture is achieved with SAR. The array configuration is designed to rotate to reduce the number of antennas. The technical feasibility of this technology is already been proven and the launch is foreseen for the near future.

Geostationary Interferometric Microwave Sounder (GIMS) is China's next generation meteorological sounder. Developed by National Space Science Center, this instrument will be launched with the FengYun-4 mission, to predict short-term weather conditions, in particular tropical cyclones [17]. Its activities of sounding temperature and humidity will be carried out by the onboard radiometer. The required resolution is satisfied both in space with rotating interferometry, as said before, and in time exploiting the geostationary orbit which should allow 15 minutes resolution as well.

(a) **GAS** scientific payload prototype [18].

(b) **GIMS** scientific payload mock-up [19].

Figure 1.4: Examples of instruments for geostationary sounder.

1.3. Onboard Instrumentation

Both **GAS** and **GIMS** GEO missions are based on the exploitation of radiometry. This technology measures the natural radiations emitted by a target object. The measurement collected in brightness temperature, in relation to a black body, is then used to retrieve other information on the studied object or even on the medium that separates it from the observer: the atmosphere. The **SMOS** mission, for instance, throughout this instrumentation recovered data on soil moisture and ocean salinity. It is also possible to observe the sea and land temperature or ocean wind speed. Moreover, microwave frequencies are mostly unaffected by weather conditions, the transparency of the cloud across these bands makes radiometry a very powerful tool for Earth Observation (EO).

A real Aperture Radiometer is a system composed of an antenna and a receiver. The first one converts the observed radiations into an electrical signal and the latter estimates the power of the voltage signal. While the receiver determines the radiometric resolution of a radiometer system, the antenna determines its spatial resolution. Interferometric radiometry (or SAR), instead, forms images of cross-correlating signals coming from multiple antennas [20]. Comparing the different voltage signals, the source direction can be computed and considering the large distances involved, the wave-front is taken as planar. In this way, the only difference between the two signals is the delay introduced by the different positions of the antennas in an array, which is designed to achieve a certain sensibility.

This length is called baseline and it is proportional to the achievable spatial resolution, as in Equation (1.1). It is similar to the one obtained by a real aperture with a diameter of the size of the baseline. Consequently, a physical aperture is synthesised [21].

$$\delta_x \propto \lambda \frac{R}{D}. \tag{1.1}$$

The spatial resolution δ_x is limited by the diffraction limit λ. Increasing the resolution means reducing δ_x. This can be done, as shown in Equation (1.1), either by reducing R, the distance between source and observer, or increasing D, the aperture diameter. Once the selected orbit is raised to geostationary altitude, the radiometer is further from the target and consequently, a larger antenna is required. The physical size of the satellite is a main constraint in the design, therefore such an aperture may only be synthesised. Another form of interferometric radiometry is using a fleet of satellites. Different geometries of spacecraft formations could reproduce a single circular aperture. Close proximity operations, if opportunely maintained, can synthesise a larger diameter.

Multi-satellite geometries, flying in formation and maintaining their relative position error below the radiometers wavelength can ensure the coherence needed in the signals in order to recover information.

This set-up has been investigated by Ahmed Kiyoshi Sugihara El Maghraby in his PhD dissertation on *Microwave Interferometric Radiometry with Satellite Formation Flight for Earth Observation* [21]. In his work, the author carries out a feasibility study of this technology. His work has been considered a baseline for this Thesis.

1.4. Control techniques for formation flying

Since formation flying dynamics will be described by exploiting ROEs, it will be shown that the system can be linearised by using mean elements. This opens up to several methods to design a controller for satellites formations. A Linear Quadratic Regulator (LQR) is developed to maintain the selected geometry.

In literature, the formation-keeping of satellite constellations has already been studied [22]. The work by Ulybyshev presents a linear-quadratic controller implementation for the formation flying of two satellites configuration [23]. It focuses on the maintenance of the spacecraft's relative position inside the constellation, while the absolute position is let to its natural evolution. This approach is effectively realised by exploiting a close-loop formulation.

Exploiting continuous formulation, the feedback control law provides the optimal control action required for minimising the in orbit relative displacements. The same approach has been followed in [24] to control a leader-follower configuration.

Moreover, optimal control is a suitable solution also for cluster formations with a centralised Chief satellite. For instance, the subject of [25] is the onboard control for a distributed system with a main central spacecraft for optical interferometry. The latest researches, on formation flight control, are now focused on continuous low-thrust control. The aim is to keep the configuration as rigid as possible and to perform minimum delta-v manoeuvres. To achieve that goal and to allow onboard guidance, relative orbital elements are exploited, as in [26].

This dissertation will include an improved perturbation model, specific for GEO, and onboard inter-satellite control will be investigated to develop a tracking control law for a larger configuration.

1.5. Scope of the Thesis

This Thesis has the objective of designing a relative motion control of a cluster formation in GEO with second-order geodetic perturbations.

Starting from those considerations on the scientific payload seen in Section 1.3, the present study developed from hereafter wishes to provide additional validation in terms of orbital mechanics and control. The aim is to merge the remote sensing advantages of interferometric radiometer using Formation Flight, with the most recent developments in terms of relative motion exploiting ROEs. An enhanced analytic dynamic model, perturbed by geopotential, up to the second-order, representing Earth's non-spherically symmetric mass distribution is developed. Then an LQR is introduced to reach the resolution requirements of the instrument embedded onboard to effectively fulfil the sounding mission in GEO.

The numerical simulation of a test case will provide a realistic scenario, to understand the behaviour of the spacecraft.

1.6. Structure of the Thesis

This dissertation goes through five chapters. The Thesis structure aims at retracing the order of the steps that have led to the presented results.

Chapter 2 presents the path followed to derive the dynamic model for the formation flight of a Chief and a Deputy satellite. Section 2.1 introduces the chosen set of relative orbital elements and how their analytic evolution is retrieved. Section 2.2 shows the numerical equation implemented for propagating the Chief's Keplerian orbital elements, taking into account geodetic perturbation up to second order. Section 2.3 merges the previous parts: obtaining a precise simulation of the orbital free evolution of the trajectories of the satellites in Subsection 2.1.3 and setting up the control matrix in Subsection 2.3.2.

Chapter 3 describes the control logic implemented for the mission. Section 3.1 defines the control problem and its requirements. In Section 3.2 the control algorithm is implemented, while in Section 3.3 a qualitative analysis of the algorithm's weighting matrices is performed. Section 3.4 performs the selection of the thrusters which best fit with the needed control effort. Finally, Section 3.5 describes how the relative position check is performed.

Chapter 4 presents the obtained results of a test case simulation. In Section 4.1, the mission is described and the initial conditions are set up. Section 4.2 shows the validation of the implemented model with already tested simulators. Finally, Section 4.3 reports all the plots resulting from the simulations.

Chapter 5, after a summary of the workflow of the study, highlights the objective achieved with this dissertation. Moreover, some insights and developments are analysed as possible future works.

This thesis is part of the COMPASS project: "Control for orbit manoeuvring by surfing through orbit perturbations" (Grant agreement No 679086).
This project is European Research Council (ERC) funded project under the European Union's Horizon 2020 research (www.compass.polimi.it).

2 | Relative system dynamics

This chapter provides a precise model of the orbital mechanics for Geostationary satellites. Starting from a review of the latest works in the relative motion prediction between two satellites (a Chief and a Deputy), the following sections try to fill the lack of a specific formulation for GEO. The majority of the studies about Formation Flying focus on LEO, where most applications are deployed [27, 28]. Thus, the researchers have focused mainly on finding a valid model for the drag and the first-order geodetic perturbations, the ones that affect most low orbits. However, when larger altitudes or particular values of eccentricity or inclination come into play, those models are not always applicable.

Hereafter relative orbital elements are introduced as selected parameters for the relative motion description, along with their derivation. Then, their relative dynamics are retrieved after having introduced the perturbations due to J_{22}. The numerical method used to obtain keplerian orbital parameters required for the ROE evolution is described. At the end of this chapter, the control matrix needed for the inclusion of the thrusters in the dynamics is derived.

2.1. Relative motion

2.1.1. Relative orbital elements

First of all, a relative state is defined. The set selection aims at fulfilling two drivers: the singularities present in GEO and the need to maintain a physical meaning in the state formulation. The quasi-nonsingular ROEs are defined in Equation (2.1)s [29]:

$$\delta\boldsymbol{\alpha} = \begin{pmatrix} \delta a \\ \delta\lambda \\ \delta e_x \\ \delta e_y \\ \delta i_x \\ \delta i_y \end{pmatrix} = \begin{pmatrix} \Delta a/a_c \\ \Delta u + \Delta\Omega\cos\left(i_c\right) \\ \Delta e_x \\ \Delta e_y \\ \Delta i \\ \Delta\Omega\sin\left(i_c\right) \end{pmatrix}, \tag{2.1}$$

where the symbol Δ represents the subtraction between the Deputy's and the Chief's orbital elements: $a,\ u,\ e_x,\ e_y,\ i,\ \Omega$, which corresponds to the semi-major axis, eccentricity, inclination, right ascension of the ascending node, and argument of perigee. The value u represents the mean argument of latitude equal to $u = \omega + M$, being M the time-dependent mean anomaly. Moreover, for the definition of $\delta\alpha$, the modified set of orbital elements is considered: $a,\ u,\ e_x,\ e_y,\ i,\ \Omega$. The components of the eccentricity vector are $e_x = e\cos(\omega)$ and $e_y = e\sin(\omega)$. While, considering the orbits of Chief and Deputy almost co-planar, the components of the relative inclination simplify as shown. This assumption is valid for $\Delta i \ll 1$ and $\Delta\Omega \ll 1$, thus trigonometry can be applied. Finally, $\delta\lambda$ denotes the relative mean longitude between the spacecraft.

The formulation provided for the relative state is referred to a two-satellite configuration. A reference Chief spacecraft, described by the subscript $\circ_c$ and the Deputy one, described by the subscript $\circ_d$. The evolution of the ROEs shows the relative motion of this latter with respect to the first one. The Deputy's position is described by a vector with origin in Chief's one and orientation given by a vector triad in the Hill coordinate frame. That recalls the typical geometric representation of two satellites' relative motion.

On the other hand, as shown in Equation (2.1), the elements are related to the well-known Keplerian elements. Those provide the satellite's position in space and the description of the orbit geometry [30].

- Semi-major axis, a, accounts for the orbit extension. It is the distance between the centre of the ellipse and one between the apoapsis or the periapsis;
- Eccentricity, e, describes how much the shape of the orbit differs from a circle. For close orbits, it is bounded: $e = 0$, circular orbit, and $e = 1$ as upper limit;
- Inclination, i, is the angle between the orbital plane and the equatorial plane;
- Right Ascension of the Ascending Node ($RAAN$), Ω, is the angle between the orbit ascending node and the Vernal equinox;
- Argument of periapsis, ω, is the angle between the periapsis and the ascending node;
- True anomaly, θ, express the angular position within the orbit of the satellite, $\theta = 0$ corresponds to the periapsis.

The last element is not the only formulation for expressing the position of a spacecraft in its orbit. Eccentric and mean anomalies are expressed relatively in Equation (2.2) and Equation (2.3).

$$E = 2 \arctan \left(\tan \left(\frac{\theta}{2} \right) \sqrt{\frac{1-e}{1+e}} \right) \tag{2.2}$$

$$M = E - e \sin (E) \tag{2.3}$$

In particular, the mean anomaly enters in Equation (2.1) in the relative mean argument of longitude $\delta\lambda$. The so-called argument of latitude $u = \omega + M$ is the sum of the argument of the periapsis and mean anomaly.

2.1.2. Hill's Cartesian to ROEs mapping

The Hill coordinate frame coincides with the more known Local-Vertical Local-Horizon (LVLH) or Radial-Tangent-Normal (RTN) frame [31]. This happens because the analysis is focused on the GEO orbits, consequently, the orbit is circular and the transversal axis coincides with the velocity vector. The frame is non-inertial, a constant rotational rate is present, which is (again due to circular orbit) the mean motion:

$$n = \sqrt{\frac{\mu}{a_C^3}},$$

where μ is the Earth's Gravitational coefficient.

In this frame, it is possible to retrieve the relative position in dimensionless coordinates. The evolution of these coordinates is described by the Hill-Clohessy-Wiltshire equations (HCW). The equations in Equation (2.4) are the result of a classical derivation obtained introducing some assumptions:

1. The magnitude of the vector representing relative position is very small in comparison with the Chief's position vector, $\Delta \boldsymbol{r} \ll \boldsymbol{r}$.
2. Pure Keplerian motion of the Chief and Deputy spacecraft.
3. Circular orbit for the Chief, $e_c = 0$ [32].

$$\begin{cases} \ddot{x} - 2n\dot{y} - 3n^2 x = 0 \\ \ddot{y} + 2n\dot{x} = 0 \\ \ddot{z} + n^2 z = 0 \end{cases} \tag{2.4}$$

where x, y and z are the components of the relative position of the previously described Hill or RTN frame. Their derivation is done with respect to a time interval Δt. Moreover, it is worth noticing the decoupling between the x y motion from the z plane. To obtain the relative position at a generic time instant t from the HCW equations, it is necessary to numerically integrate them starting from an initial condition $\mathbf{X}(\mathbf{t} = \mathbf{t_0}) = \{x, y, z, \dot{x}, \dot{y}, \dot{z}\}'$. The general closed-form solution is represented in matrix form in equation Equation (2.5).

$$\begin{pmatrix} x(t) \\ y(t) \\ z(t) \\ \dot{x}(t) \\ \dot{y}(t) \\ \dot{z}(t) \end{pmatrix} = \begin{bmatrix} 1 & 0 & -\cos(t) & -\sin(t) & 0 & 0 \\ -\frac{3}{2}(t - t_0) & 1 & 2\sin(t) & -2\cos(t) & 0 & 0 \\ 0 & 0 & 0 & 0 & \sin(t) & -\cos(t) \\ 0 & 0 & \sin(t) & -\cos(t) & 0 & 0 \\ -\frac{3}{2} & 0 & 2\cos(t) & 2\sin(t) & 0 & 0 \\ 0 & 0 & 0 & 0 & \cos(t) & \sin(t) \end{bmatrix} \cdot \begin{pmatrix} k_1 \\ k_2 \\ k_3 \\ k_4 \\ k_5 \\ k_6 \end{pmatrix} \tag{2.5}$$

Depending on the chosen initial condition, different integration constants k_i are retrieved; the relation between them is expressed in Equation (2.6).

$$\begin{cases} k_1 = 4x_0 + 2\dot{y}_0 \\ k_2 = x_0 - 2\dot{x}_0 \\ k_3 = 3x_0 + 2\dot{y}_0 \\ k_4 = -\dot{x}_0 \\ k_5 = \dot{z}_0 \\ k_6 = -z_0 \end{cases} \tag{2.6}$$

The complete set of Cartesian elements is characterised by the fast variation of its elements. This feature results in significant computational effort when integrating it during a simulation. Another drawback is the lack of a simple physical interpretation of the relative motion. To overcome these problems, different approaches have been tested, starting for example from the set of coordinates. For example, the implementation of ROEs brings

numerous advantages. In the first place, there is a set of quasi-nonsingular and nonsingular ROEs that are suitable for GEO orbits and close-proximity operations. Moreover, through mathematical manipulations, it is possible to transform a differential problem into an algebraic one, exploiting the fact that only one of its elements varies quickly. Solving an equation is more computationally efficient than numerical integration. All these features make ROEs a more flexible choice.

The path for the HCW equations transformation in the ROE formulation goes through Gauss' variational equations. They represent the motion in terms of orbital elements (the Keplerian previously described) variation. For unperturbed motion, only one element has a non-null rate of variation: the true anomaly and consequently the same happens for the mean anomaly. All the others are considered constant. In an environment in which both eccentricity and inclination are close to zero, such as GEO with circular and near-equatorial orbit, for avoiding singularities, the equations are expressed using a set of modified orbital elements: $\{a, u, e_x, e_y, i, \Omega\}'$. When perturbing forces are taken into account, the orbital elements are subjected to acceleration and their behaviour is no longer constant. The matricial form in Equation (2.7) reports the Gauss' equations with respect to a dimensionless perturbing acceleration $\mathbf{d} = \{d_R, d_T, d_N\}'$ expressed in the RTN frame [32].

$$\begin{pmatrix} \dot{a} \\ \dot{u} \\ \dot{e_x} \\ \dot{e_y} \\ \dot{i} \\ \dot{\Omega} \end{pmatrix} = \begin{bmatrix} 0 & 0 & 2a & 0 \\ 1 & -2 & 0 & -\dfrac{\sin(t)}{\tan(i)} \\ 0 & \sin(t) & 2\cos(t) & 0 \\ 0 & -\cos(t) & 2\sin(t) & 0 \\ 0 & 0 & 0 & \cos(t) \\ 0 & 0 & 0 & \dfrac{\sin(t)}{\sin(i)} \end{bmatrix} \cdot \begin{pmatrix} 1 \\ d_R \\ d_T \\ d_N \end{pmatrix} \tag{2.7}$$

To obtain the change of the orbital elements due to an instantaneous velocity variation, the integration of the previously described equations is performed in the neighbourhood of $t = t_0$, for example. As aforementioned, implementing a quasi-nonsingular ROE formulation, the relative motion is introduced. As an integration result, $\mathbf{d}$ becomes a dimensionless Δv. Consequently, the formulation in Equation (2.8) highlights how an instantaneous variation of velocity in different directions of the RTN frame affects the variation of the orbital elements. In particular, fluctuations in tangential velocity are responsible for orbit changes in shape ($\Delta a, \Delta e_x$ & Δe_y). On the other hand, normal velocity variations only affect the argument of latitude and the relative inclination vector ($\Delta u, \Delta i_x$ & Δi_y).

Finally, Δu can be expressed as in Equation (2.9).

$$\begin{pmatrix} \Delta a/a \\ \Delta u \\ \Delta e_x \\ \Delta e_y \\ \Delta i_x \\ \Delta i_y \end{pmatrix} = \begin{bmatrix} 0 & 2 & 0 \\ -2 & 0 & -\dfrac{\sin(t)}{\tan(i)} \\ \sin(t) & 2\cos(t) & 0 \\ -\cos(t) & 2\sin(t) & 0 \\ 0 & 0 & \cos(t) \\ 0 & 0 & \dfrac{\sin(t)}{\sin(i)} \end{bmatrix} \cdot \begin{pmatrix} \Delta v_R \\ \Delta v_T \\ \Delta v_N \end{pmatrix} \tag{2.8}$$

$$\begin{aligned} \Delta u &= -2\Delta v_R - \frac{\sin(t_0)}{\tan(i)}\Delta v_N = -2\Delta v_R - \frac{\Delta i_y}{\tan(i)} = \\ &= -2\Delta v_R - \frac{\Delta\Omega \sin(i)}{\tan(i)} = -2\Delta v_R - \Delta\Omega\cos(i) \end{aligned} \tag{2.9}$$

Starting from a single spacecraft evolution, this approach can be used for two satellite configurations. If the same initial condition is assumed for both satellites, let's call them Chief and Deputy, no relative motion is introduced. If the Deputy's state is perturbed, a description of the formation flying is provided. In other words, Equation (2.8) maps different initial states into a change of the orbital elements.

Once retrieved the Gauss' equations including relative motion, is possible to write the new HCW equations aiming at replacing the integration constants with ROEs, to benefit from their previously described advantages. For expressing $\mathbf{k}$ explicitly as in Equation (2.10), it is necessary to invert the matrix in Equation (2.5). After that, the complexity and the size of the problem are reduced in Equation (2.11) by assuming $t = t_0$ and the origin as the initial position of the state [33]. Those assumptions are specifically designed to introduce a relative motion in the formulation.

$$\begin{pmatrix} k_1 \\ k_2 \\ k_3 \\ k_4 \\ k_5 \\ k_6 \end{pmatrix} = \begin{bmatrix} 4 & 0 & 0 & 0 & 2 & 0 \\ 6(t-t_0) & 1 & 0 & -2 & 3(t-t_0) & 0 \\ 3\cos(t) & 0 & 0 & \sin(t) & 2\cos(t) & 0 \\ 3\sin(t) & 0 & 0 & -\cos(t) & 2\sin(t) & 0 \\ 0 & 0 & \sin(t) & 0 & 0 & \cos(t) \\ 0 & 0 & -\cos(t) & 0 & 0 & \sin(t) \end{bmatrix} \cdot \begin{pmatrix} x(t) \\ y(t) \\ z(t) \\ \dot{x}(t) \\ \dot{y}(t) \\ \dot{z}(t) \end{pmatrix} \tag{2.10}$$

$$\begin{pmatrix} k_1 \\ k_2 \\ k_3 \\ k_4 \\ k_5 \\ k_6 \end{pmatrix} = \begin{bmatrix} 0 & 2 & 0 \\ -2 & 0 & 0 \\ \sin(t_0) & 2\cos(t_0) & 0 \\ -\cos(t_0) & 2\sin(t_0) & 0 \\ 0 & 0 & \cos(t_0) \\ 0 & 0 & \sin(t_0) \end{bmatrix} \cdot \begin{pmatrix} \dot{x}(t_0) \\ \dot{y}(t_0) \\ \dot{z}(t_0) \end{pmatrix} \tag{2.11}$$

Therefore, by replacing the integration constants with the ROEs, relative motion can be introduced. The substitutions, performed in Equation (2.12), make clear that only k_2 has a time dependency, $\Delta u(t)$. To keep it constant, as expected for an integration constant, it particularised for $t = t_0$.

$$\begin{cases} k_1 = (a_d - a_c)/a_c = \Delta a/a \\ k_2 = [u_d(t) - u_c(t)] + (\Omega_d - \Omega_c)\cos(i_c) = \Delta u_0 + \Delta\Omega\cos(i) \\ k_3 = e_{x_d} - e_{x_c} = \Delta e_x \\ k_4 = e_{y_d} - e_{y_c} = \Delta e_y \\ k_5 = i_d - i_c = \Delta i_x \\ k_6 = e_{x_d} - e_{x_c} = \Delta i_y \end{cases} \tag{2.12}$$

By replacing Equation (2.12) into Equation (2.5), it is possible to obtain a system of linear equations, shown in Equation (2.13) which link ROEs to relative Cartesian elements:

$$\begin{cases} x/a = \delta a - \delta e_x\cos(u) - \delta e_y\sin(u) \\ y/a = -\delta\lambda_0 - \dfrac{3}{2}\delta a(u - u_0) - 2\delta e_y\cos(u) + 2\delta e_x\sin(u) \\ z/a = -\delta i_y\cos(u) + \delta i_x\sin(u) \\ v_x/v = -\delta e_y\cos(u) + \delta e_x\sin(u) \\ v_y/v = -\dfrac{3}{2}\delta a + 2\delta e_x\cos(u) + 2\delta e_y\sin(u) \\ v_z/v = \delta i_x\cos(u) + \delta i_y\sin(u) \end{cases} \tag{2.13}$$

where $v = n \cdot a$ is the Chief's characteristic velocity. Finally the mapping tool between Hill's Cartesian coordinates and ROEs is set by merging Equation (2.10) and Equation (2.12) and reported in Equation (2.14).

$$\begin{pmatrix} \Delta a/a \\ \Delta u \\ \Delta e_x \\ \Delta e_y \\ \Delta i_x \\ \Delta i_y \end{pmatrix} = \begin{bmatrix} 4 & 0 & 0 & 0 & 2 & 0 \\ 0 & 1 & 0 & -2 & 0 & 0 \\ 3\cos(u) & 0 & 0 & \sin(u) & 2\cos(u) & 0 \\ 3\sin(u) & 0 & 0 & -\cos(u) & 2\sin(u) & 0 \\ 0 & 0 & \sin(u) & 0 & 0 & \cos(u) \\ 0 & 0 & -\cos(u) & 0 & 0 & \sin(u) \end{bmatrix} \cdot \begin{pmatrix} x/a \\ y/a \\ z/a \\ v_x/v \\ v_y/v \\ v_z/v \end{pmatrix} \tag{2.14}$$

2.1.3. Analytical model

Following the framework definition, the analytical model for the relative motion description in ROEs is presented. The only effect considered in the propagation of the satellites is due to the geodetic potential. Many works, focusing on LEO, have taken into account drag or oblateness perturbations; without going further in the analysis of the higher orders. Since at geostationary altitude second-order term plays a significant role, this work goes in that direction exploiting a study carried out by Gais et al. and developing a model for orbital perturbation due to Earth's non-spherically symmetric mass distribution [34].

That work presents an analytical model based on a State Transition Matrix (STM) to carry out precise relative motion, for low altitudes. Exploiting a convenient transformation between osculating and mean ROE, the matrix shown in Equation (2.15) allows compute the evolution of two spacecraft with high computing efficiency. The adopted transformation is the one retrieved from the Brouwer's generating functions by Gim and Alfriend. Working with mean relative orbital elements only accounts for the secular evolution, avoiding short- and long-term variations which lead to a more complex control. The assembling of the state transition matrix takes into account the Earth's geopotential up to the p order: $\mathbf{J} = \{J_0,\ J_2,\ J_{22},\ J_4,\ \ldots,\ J_p\}$.

$$\Phi(\alpha_{\mathbf{c}}, \mathbf{\Delta t}) = \tag{2.15}$$

$$\begin{bmatrix} 1 & 0 & 0 & 0 & 0 & 0 \\ a\Delta t \sum_p g_a^{(p)} & 1 & \sum_p g_{e_x}^{(p)} & \Delta t \sum_p g_{e_y}^{(p)} & \Delta t \sum_p g_i^{(p)} & 0 \\ a\Delta t A_1 \sum_p \dot{\omega}_a^{(p)} & 0 & C + \Delta t A_1 \sum_p \dot{\omega}_{e_x}^{(p)} & -S + \Delta t A_1 \sum_p \dot{\omega}_{e_y}^{(p)} & \Delta t A_1 \sum_p \dot{\omega}_i^{(p)} & 0 \\ a\Delta t A_2 \sum_p \dot{\omega}_a^{(p)} & 0 & S + \Delta t A_2 \sum_p \dot{\omega}_{e_x}^{(p)} & C + \Delta t A_2 \sum_p \dot{\omega}_{e_y}^{(p)} & \Delta t A_2 \sum_p \dot{\omega}_i^{(p)} & 0 \\ 0 & 0 & 0 & 0 & 1 & 0 \\ a\sin(i)\Delta t \sum_p \dot{\Omega}_a^{(p)} & 0 & \sin(i)\Delta t \sum_p \dot{\Omega}_{e_x}^{(p)} & \sin(i)\Delta t \sum_p \dot{\Omega}_{e_y}^{(p)} & \sin(i)\Delta t \sum_p \dot{\Omega}_i^{(p)} & 1 \end{bmatrix}$$

Where $\circ_x^{(p)}$ stands for the respective partial derivative of the J_p contribution with respect to x. While the other functions are listed below:

- $A1 = -(Se_{x_0} + Ce_{y_0})$;
- $A2 = (Ce_{x_0} + Se_{y_0})$;
- $S = \sin\left(\sum_p \dot{\omega}^{p)} \Delta t\right)$;
- $C = \cos\left(\sum_p \dot{\omega}^{p)} \Delta t\right)$.
- $g = \dot{\omega} + \dot{M} + \dot{\Omega}\cos(i)$.

With this formulation, the level of accuracy of the model follows the mission requirements. Once assembled, the STM is used to analytically compute the ROE evolution at a certain time by knowing the initial condition and the Chief's Keplerian orbital elements $\alpha_\mathbf{c}$ at that time. The generic formulation, expressed in Equation (2.16), sets the basis for the control problem. As the dynamic model is controlled continuously the evolution must as well match that. In the following sections, both this and the Chief propagation are carried out.

$$\delta\alpha(t_0 + \Delta t) = \Phi(\alpha_\mathbf{c}, \Delta t) \cdot \delta\alpha_\mathbf{0} \tag{2.16}$$

2.2. Chief propagation

As aforementioned, a constant update must be performed for the computation of the Chief's orbital elements. The two-body problem with conservative perturbations can be solved by numerical integration in Cartesian coordinates or using the Keplerian elements by using the Gauss' Planetary Equations. The integration is performed with *MATLAB* solver `ode113` with a relative tolerance of 10^{13} and absolute tolerance of 10^{14}. `ode113` is a variable-step, variable-order (VSVO) Adams-Bashforth-Moulton solver of orders 1 to 13 [35]. It is adopted because it is more efficient than other solvers at stringent tolerances or when the differential function is particularly expensive to evaluate.

2.2.1. Gravitational perturbations

There are different sources of orbital perturbations. At lower altitudes, the Earth's oblateness, the drag and the magnetic field perturbations prevail. In GEO, the third bodies and the Solar Radiation Pressure start to play a major role as well. This work focuses only on the geodetic effect. The Earth's oblate spheroid shape produces a slightly different gravitational field than the one of a perfect sphere. A perturbing acceleration accounting for that conservative force has to be included in the propagation. This latter is retrieved, in Cartesian form, from the derivation of the true gravitational field that is expressed as a series of spherical harmonics.

The selected model, taken from the literature, is based on a potential function R accounting for the non-Keplerian motion and expressed in Equation (2.17) [36].

$$R = \frac{\mu}{r} \sum_{l=2}^{\infty} \sum_{m=0}^{l} \left(\frac{R_{\oplus}}{r} \right)^{l} P_{l,m} \sin(\phi_c) [C_{l,m} \cos(m\lambda_c) + S_{l,m} \sin(m\lambda_c)] \tag{2.17}$$

Where r is the distance of the satellite, $R_{\oplus}$ is the equatorial Earth's radius, $P_{l,m}$ are the Legendre polynomials, ϕ_c and λ_c are the geocentric latitude and longitude of the Chief and $C_{l,m}$ and $S_{l,m}$ are the harmonic coefficients that could be derived or found tabulated. The selected model takes into account all zonal tesseral and sectorial harmonics. Regarding the former, it includes J_2, the first secular effect with $m = 0$. For the latter, with a lower relevance but still present, also the terms referred to m, l up to order 2 are introduced.

The Cartesian components of the acceleration are retrieved by deriving the spherical potential (up to the second harmonics) and then transposing them in another frame following the formulations shown in Equation (2.18) and Equation (2.19) [37].

$$\begin{cases} d_x = \dfrac{\partial R}{\partial r} \cdot \dfrac{\partial r}{\partial x} + \dfrac{\partial R}{\partial \phi} \cdot \dfrac{\partial \phi}{\partial x} + \dfrac{\partial R}{\partial \lambda} \cdot \dfrac{\partial \lambda}{\partial x} \\ d_y = \dfrac{\partial R}{\partial r} \cdot \dfrac{\partial r}{\partial y} + \dfrac{\partial R}{\partial \phi} \cdot \dfrac{\partial \phi}{\partial y} + \dfrac{\partial R}{\partial \lambda} \cdot \dfrac{\partial \lambda}{\partial \partial y} \\ d_z = \dfrac{\partial R}{\partial r} \cdot \dfrac{\partial r}{\partial z} + \dfrac{\partial R}{\partial \phi} \cdot \dfrac{\partial \phi}{\partial z} + \dfrac{\partial R}{\partial \lambda} \cdot \dfrac{\partial \lambda}{\partial z} \end{cases} \tag{2.18}$$

$$\begin{cases} \dfrac{\partial r}{\partial x} = \dfrac{x}{r} \\ \dfrac{\partial r}{\partial y} = \dfrac{y}{r} \\ \dfrac{\partial r}{\partial z} = \dfrac{z}{r} \end{cases} \qquad \begin{cases} \dfrac{\partial \phi}{\partial x} = -\dfrac{x \cdot z}{r^3 \sqrt{1 - \dfrac{z^2}{r^2}}} \\ \dfrac{\partial \phi}{\partial y} = -\dfrac{y \cdot z}{r^3 \sqrt{1 - \dfrac{z^2}{r^2}}} \\ \dfrac{\partial \phi}{\partial z} = -\dfrac{\dfrac{z^2}{r^3} - \dfrac{1}{r}}{\sqrt{1 - \dfrac{z^2}{r^2}}} \end{cases} \qquad \begin{cases} \dfrac{\lambda}{x} = \dfrac{-y}{x^2 \left(1 + \dfrac{y^2}{x^2}\right)} \\ \dfrac{\lambda}{y} = \dfrac{1}{x \left(1 + \dfrac{y^2}{x^2}\right)} \\ \dfrac{\lambda}{z} = 0 \end{cases} \tag{2.19}$$

Where $(r,\ \phi,\ \lambda)$ are spherical coordinates, representing respectively the radius, the latitude and the longitude. While $(x,\ y,\ z)$ are the Cartesian ones.

2.2.2. Integration methods

Cartesian Coordinates

The components of the perturbing accelerations are evaluated for each direction and the Cartesian state vector derivative is computed accordingly to Equation (2.20) [38].

$$\frac{d}{dt}\begin{Bmatrix}\mathbf{r}\\ \mathbf{v}\end{Bmatrix} = \begin{Bmatrix}\mathbf{v}\\ -\frac{\mu}{r^3}\mathbf{r}+\mathbf{d}\end{Bmatrix} \tag{2.20}$$

Gauss' Planetary Equations

The Cartesian components of the perturbing accelerations are evaluated and then converted to RTN components and the Keplerian elements evolution is computed accordingly to Equation (2.21) [38].

$$\begin{cases}\dot{a} = 2a^2\dfrac{v}{\mu}d_T\\ \dot{e} = 2\dfrac{d_T}{v}(e+\cos f)\\ \dot{i} = r\cos(f)\dfrac{d_R}{h}\\ \dot{\Omega} = r\sin(f)\dfrac{d_R}{h\sin(i)}\\ \dot{\omega} = \dfrac{2d_T\sin(\theta)}{e\cdot v} + d_N\left(2e+\dfrac{r}{a}\cos(\theta)\right) - r\sin(f)\dfrac{d_R}{h\sin(i)}\cos(i)\\ \dot{\theta} = \dfrac{h}{r^2} - \dfrac{2d_T\sin(\theta)}{e\cdot v} + d_N\left(2e+\dfrac{r}{a}\cos(\theta)\right)\end{cases} \tag{2.21}$$

2.3. System evolution

Finally, the set-up of the dynamical equations of the problem is presented. In this direction, it is necessary to include the natural evolution of the relative motion, as well as the control action. The final formulation is in matricial form, merging all the previous models retrieved in Subsection 2.1.3.

2.3.1. State Transition Matrix

As shown before, it is possible to retrieve the relative motion for every time instant only knowing the initial condition, the Chief's updated state and the time instant. The implementation of a linear system allows, as said before, high computational efficiency and accuracy [39]. The derivation of STMs can be carried out from the time derivative of the relative state, as in Equation (2.23). Writing the Deputy's state as a function of Chief's one, it is evident that the requirement is fulfilled: $\delta\dot{\alpha} = \mathbf{f}(\alpha_{\mathbf{d}}(\alpha_{\mathbf{c}}(\mathbf{t})), \alpha_{\mathbf{c}}(\mathbf{t}), \gamma)$; with γ representing all the others parameters required to include perturbations. The derivation of the STM in Equation (2.15), is valid as a perturbed ROE dynamics as long as it is linearised at the first order of Taylor's expansion expressed in [40].

$$\mathbf{A}(\alpha_{\mathbf{c}}, \gamma) = \left.\frac{\partial \delta\dot{\alpha}}{\partial \delta\alpha_{\mathbf{d}}}\right|_{\partial\delta\alpha=0} \cdot \left.\frac{\partial \alpha_{\mathbf{d}}}{\partial \delta\alpha_{\mathbf{d}}}\right|_{\alpha_{\mathbf{d}}=\alpha_{\mathbf{c}}} \tag{2.22}$$

Equation (2.23) describes the temporal derivative of Equation (2.16). It highlights that it is approximated as a linear function and the resulting STM $\boldsymbol{A}$ is then assembled as in Equation (2.24).

$$\delta\dot{\alpha} = A(\alpha_{\mathbf{c}}(\mathbf{t}), \gamma) \cdot \delta\alpha(t) + \mathcal{O}(\delta\alpha^2) \tag{2.23}$$

$$\mathbf{A}(\delta\alpha_{\mathbf{c}}) \approx \tag{2.24}$$

$$\approx \begin{bmatrix} 0 & 0 & 0 & 0 & 0 & 0 \\ a\sum_p g_a^{(p)} & 0 & \sum_p g_{e_x}^{(p)} & \sum_p g_{e_y}^{(p)} & \sum_p g_i^{(p)} & 0 \\ aA_1\sum_p \dot{\omega}_a^{(p)} & 0 & C + A_1\sum_p \dot{\omega}_{e_x}^{(p)} & -S + A_1\sum_p \dot{\omega}_{e_y}^{(p)} & A_1\sum_p \dot{\omega}_i^{(p)} & 0 \\ aA_2\sum_p \dot{\omega}_a^{(p)} & 0 & S + A_2\sum_p \dot{\omega}_{e_x}^{(p)} & C + A_2\sum_p \dot{\omega}_{e_y}^{(p)} & A_2\sum_p \dot{\omega}_i^{(p)} & 0 \\ 0 & 0 & 0 & 0 & 0 & 0 \\ a\sin(i)\sum_p \dot{\Omega}_a^{(p)} & 0 & \sin(i)\sum_p \dot{\Omega}_{e_x}^{(p)} & \sin(i)\sum_p \dot{\Omega}_{e_y}^{(p)} & \sin(i)\sum_p \dot{\Omega}_i^{(p)} & 0 \end{bmatrix}$$

The plant matrix of system A includes the property of Subsection 2.1.3 and accounts for geodetic perturbation up to the J_{22} effect. The partial derivatives of the orbital elements are computed from the literature classical formulation in Equation (2.25).

$$\dot{\Omega} = -\frac{3}{2}J_2 n \left(\frac{R_\oplus}{a}\right)^2 \frac{\cos(i)}{(1-e^2)^2} + \dots \tag{2.25a}$$
$$+ \frac{J_{22}}{(1-e^2)^4}\left(\frac{R_\oplus}{a}\right)^4 \cos(i)\left[\left(\frac{-45}{8}+\frac{3}{4}e^2+\frac{9}{32}e^4\right)+\left(\frac{57}{8}-\frac{69}{32}e^2+\frac{27}{64}e^4\right)\sin(i)^2\right]$$

$$\dot{\omega} = \frac{3}{4}J_2 n \left(\frac{R_\oplus}{a}\right)^2 \frac{5\cos(i)^2-1}{(1-e^2)^2} + \dots \tag{2.25b}$$
$$+ \frac{J_{22}}{(1-e^2)^4}\left(\frac{R_\oplus}{a}\right)^4 \left[\left(\frac{27}{2}-\frac{15}{16}e^2-\frac{9}{16}e^4\right)+\dots\right.$$
$$\left.+\left(\frac{507}{16}+\frac{171}{32}e^2+\frac{99}{64}e^4\right)\sin(i)^2+\left(\frac{1185}{64}-\frac{675}{128}e^2-\frac{135}{128}e^4\right)\sin(i)^4\right]$$

$$\dot{M} = n + \frac{3}{4}J_2 n \left(\frac{R_\oplus}{a}\right)^2 \frac{3\cos(i)^2-1}{\sqrt{(1-e^2)^3}} + \dots \tag{2.25c}$$
$$- \frac{J_{22}}{\sqrt{(1-e^2)^7}}\left(\frac{R_\oplus}{a}\right)^4 \left(\frac{5}{64}\right)(2-e^2)\sin(i)$$

The full expression of Equation (2.24), including the partial derivatives of Keplerian elements, is provided in appendix A.

2.3.2. Control matrix

Finally, the control action is introduced in the system dynamics. A set of thrusters provides the required acceleration to perform the cluster formation maintenance. Usually, the actuators are oriented along the satellite body axes. In this thesis, it is considered that only the Deputies perform control for formation maintenance. To guarantee that the actuators are providing the thrust in the correct direction, the attitude of the Deputies is considered rigid and its formulation is not included in the control model. Consequently, the controlling accelerations are described in the RTN frame. Thus, it becomes crucial to define a transformation to link those components in the RTN frame with the ROE state. This operation is carried out by the control matrix $\mathbf{B}$, reported in Equation (2.26) [41]. In Subsection 2.1.2 the relation between these different frames has been described, exploiting Gauss' Planetary Equations and a hint of what is needed is given in Equation (2.8).

While previously a dimensionless formulation could have been useful, now accelerations with their unit lead to a slight modification for the control matrix derivation. The mean argument of the latitude u has replaced the time information as shown with the mapping in Equation (2.14). The tightness of the formation implicitly imposes that $a_d/a_c \approx 1$, allowing a simplification, the same happens for $\Delta i \ll 1$, assuring the assumptions associated with Equations (2.8) and (2.11). The accelerations act only on the Deputy, the Chief's orbital elements are considered constant to obtain the matrix $\mathbf{B}$.

$$\mathbf{B}(\alpha_{\mathbf{c}}) = \frac{1}{n \cdot a} \begin{bmatrix} 0 & 2 & 0 \\ -2 & 0 & 0 \\ \sin(u) & 2\cos(u) & 0 \\ -\cos(u) & 2\sin(u) & 0 \\ 0 & 0 & \cos(u) \\ 0 & 0 & \sin(u) \end{bmatrix} \tag{2.26}$$

The presented matrix evaluates how three independent and orthogonal control accelerations influence the ROEs, to achieve the goal imposed by the control logic.

2.3.3. Problem set-up

Merging the matrices obtained in Subsections 2.3.1 and 2.3.2, the complete system dynamic model is computed in Equation (2.27) [42]:

$$\delta\dot{\alpha} = \mathbf{A}(\delta\alpha) + \mathbf{B}\mathbf{u} \tag{2.27}$$

where matrix $\mathbf{A}$ accounts for the natural propagation of the relative motion due to Earth's geopotential perturbation, while $\mathbf{B}$ allows performing an active control on the orbit. The vectors, on one hand, represent the evolution of the ROEs, described by the $\delta\alpha$. On the other hand, $\mathbf{u}$ represents the control accelerations and it is computed by the control algorithm at each time step.

3 | Continuous feed-back control

The aim of this chapter is the implementation of a control logic to maintain the cluster formation rigid. Consequently, a steady-state linear quadratic regulator is tuned to the linear system described in Chapter 2. Moreover, a brief analysis of the eligible thrusters and physical constraints which should be considered when talking about formation flight is presented.

The use of the dynamic model, retrieved in Chapter 2 with the analytic framework, together with the miniaturisation of the required computational tools allows the development of an on-board control. The magnitude of the estimated Δv provides a hint of the control effort needed and so the selection of the actuators comes as a consequence.

3.1. Control logic

This dissertation is focused on the relative motion of a cluster formation and, for this reason, the focus is on formation-keeping. The uncontrolled propagation leads to significant deviation, due to the external perturbation, including the geodetic one. This behaviour affects the maintenance of the geometry of the fleet and the possibility to satisfy the required accuracy from the combined interferometry point of view. The cluster should maintain a tight and rigid geometry to reach a certain spatial resolution.

The continuous evolution of the orbital parameters together with the strict requirements in the relative position is not suitable for impulsive manoeuvres. A more practical and effective solution is the implementation of continuous feedback control. A closed-loop algorithm takes as input the reference orbit and compares it with the actual state. For the simulator used in this thesis, the analytical formulation based on ROEs is adopted, but in a real environment, the sensors can provide the estimated relative position. The described model can be introduced in a Kalman filter for the inter-satellite positions.

At each time step, based on this information, the controller computes the optimal actuation forces for each Deputy. Throughout a continuous control action, the formation geometry is maintained. The state vectors are assumed to be known exactly, the uncertainties of the sensors are not considered and thrusters do not introduce noise. In this way, the delivered control action can be arbitrary and the feedback control is considered ideal.

The control logic, presented from here on, computes the forces required from the Deputies to keep a rigid formation. The Chief is allowed to drift, but the control of the position of the whole constellation in GEO is also required. The spacecraft shall remain in the specified GEO slot. The importance of managing that requirement is vital. Many different satellites populate the GEO belt, therefore interference and collision must be avoided. The station-keeping for geostationary orbit is usually performed once per month. An already validated and employed technique is the East-West Station Keeping (EWSK) [43]. This method exploits the natural evolution due to the Earth's gravity perturbation. By formulating the equation of motion in Earth's fixed polar coordinates radium, longitude and latitude $(r,\ \lambda,\ \phi)$, it is possible to visualise in phase-space that the satellite longitude varies around the equilibria points. An impulsive manoeuvre is performed when λ reaches the slot limit, then the main perturbation due to J_{22} counteracts that actuation until the spacecraft again "hits" the longitude dead-band boundary. This operation does not fit in the time scales involved in the studied mission profile, that is why station-keeping is necessary but not taken into account in this work [43].

3.2. LQR algorithm

The Linear Quadratic Regulator is a control algorithm belonging to the *Optimal Control* theory. It solves problems described by a linear set of differential equations by minimising a quadratic cost function (LQ problems).

3.2.1. Method definition

The Equation (3.1) is an example of a linear time-varying (LTI) system.

$$\dot{\boldsymbol{x}} = \boldsymbol{A}(t)\boldsymbol{x} + \boldsymbol{B}(t)\boldsymbol{u} \tag{3.1}$$

The variation of the state vector $\dot{\boldsymbol{x}}$ is expressed with respect to the state itself $\boldsymbol{x}$, multiplied by the linear plant matrix $\boldsymbol{A}(t)$ describing the system evolution, and the control vector $\boldsymbol{u}$ properly transformed by control matrix $\boldsymbol{B}(t)$.

To find the optimal control, the quadratic cost function to be minimised is shown in Equation (3.2), for LQR theory [44].

$$J(t_0) = \frac{1}{2}\boldsymbol{x}^T(t_f)\boldsymbol{M}(t_f)\boldsymbol{x}(T) + \frac{1}{2}\int_{t_0}^{t_f}(\boldsymbol{x}^T\boldsymbol{Q}(t)\boldsymbol{x} + \boldsymbol{u}^T\boldsymbol{R}(t)\boldsymbol{u})dt \tag{3.2}$$

To optimise the control action, needed by the linear system in the interval $[t_0,\ t_f]$, the information on both the initial and final state should be available. Moreover, it is necessary to introduce three weighting matrices. These are all positive semi-definite and symmetric in their interval of interest. The matrix $\boldsymbol{M}$ is the result of a differential equation, while $\boldsymbol{Q}$ and $\boldsymbol{R}$ have to be tuned aiming at accomplishing the requirements.

- $\boldsymbol{M}$, comes out solving Riccati's equation. It plays a key role in the computation of the control vector composing the gain matrix.
- $\boldsymbol{Q}$, modulates the effect of each component of the state vector in the cost function. Therefore to reduce the error on a specific element, it is necessary to increase the corresponding elements in $\boldsymbol{Q}$.
- $\boldsymbol{R}$, modulates the effect of each component of the control vector in the cost function. Therefore to reduce the effect of a specific control element, it is necessary to increase the corresponding elements in $\boldsymbol{R}$.

To make the expression for optimal control explicit, let's exploit the Hamiltonian, in Equation (3.3), associated with the plant matrix [44]:

$$H(t) = \frac{1}{2}(\boldsymbol{x}^T\boldsymbol{Q}\boldsymbol{x} + \boldsymbol{u}^t\boldsymbol{R}\boldsymbol{u}) + \boldsymbol{\lambda}^{\boldsymbol{T}}(\boldsymbol{A}(t)\boldsymbol{x} + \boldsymbol{B}(t)\boldsymbol{u})\ , \tag{3.3}$$

where H is the Legendre transformation of the Lagrangian and it is defined through a set of costate variables λ. The partial derivatives of this function with respect to their coordinates give a set of differential equations, which returns the temporal evolution of the system.

The set reported in Equation (3.4) is composed of the Hamiltonian equations.

$$\dot{\boldsymbol{x}}(t) = \frac{\partial H(t)}{\partial \boldsymbol{\lambda}} = \boldsymbol{A}(t)\boldsymbol{x} + \boldsymbol{B}\boldsymbol{u} \tag{3.4a}$$

$$-\dot{\boldsymbol{\lambda}} = \frac{\partial H}{\partial \boldsymbol{x}} = \boldsymbol{Q}\boldsymbol{x} + \boldsymbol{A}^T\boldsymbol{\lambda} \tag{3.4b}$$

$$\boldsymbol{0} = \frac{\partial H}{\partial \boldsymbol{u}} = \boldsymbol{R}\boldsymbol{u} + \boldsymbol{B}^T\boldsymbol{\lambda} \tag{3.4c}$$

Rewriting Equation (3.4c), the expression of the optimal control is retrieved and reported in Equation (3.5) in terms of the costate variables.

$$\boldsymbol{u}(t) = -\boldsymbol{R}^{-1}\boldsymbol{B}^T\boldsymbol{\lambda} \tag{3.5}$$

Replacing Equation (3.5) in Equation (3.4b), the matricial formulation of the Hamiltonian system can be expressed as in Equation (3.6).

$$\begin{pmatrix} \dot{\boldsymbol{x}} \\ \dot{\boldsymbol{\lambda}} \end{pmatrix} = \begin{bmatrix} \boldsymbol{A} & \boldsymbol{B}\boldsymbol{R}^{-1}\boldsymbol{B}^T \\ -\boldsymbol{Q} & -\boldsymbol{A}^T \end{bmatrix} \begin{pmatrix} \boldsymbol{x} \\ \boldsymbol{\lambda} \end{pmatrix} \tag{3.6}$$

Because of the remarkable evolution of the ROEs, the rate of change of the matrix $\dot{\boldsymbol{M}} \not\approx 0$ shall not be considered small. Therefore the only suitable approach to solve the problem is through *Differential Riccati's Equation*. The differential form is the one corresponding to the *Finite Horizon*, whereby the final time t_f has a finite value. At this last time step, the actual state has to match the desired one $\boldsymbol{x}(t_f) = \boldsymbol{x_d}$. Now the problem is boundary-valued. To retrieve the intermediate matrix $\boldsymbol{M}$, essential for computing the vector $\boldsymbol{u}$, let's assume the relation expressed in Equation (3.7) to be linear[22].

$$\boldsymbol{\lambda}(t) = \boldsymbol{M}(t)\boldsymbol{x}(t) \tag{3.7}$$

Then, Equation (3.8) is computed by differentiating Equation (3.7) [45].

$$\dot{\boldsymbol{\lambda}} = \dot{\boldsymbol{M}}(t)\boldsymbol{x}(t) + \boldsymbol{M}(t)\dot{\boldsymbol{x}}(t) = \dot{\boldsymbol{M}}(t)\boldsymbol{x}(t) + \boldsymbol{M}(\boldsymbol{A}\boldsymbol{x} - \boldsymbol{B}\boldsymbol{R}^{-1}\boldsymbol{B}^T\boldsymbol{M}\boldsymbol{x}) \tag{3.8}$$

For obtaining the *Differential Riccati's Equation*, let's replace $\dot{\boldsymbol{\lambda}}$ with Equation (3.4b) and the costate variable with the relation in Equation (3.7). Equation (3.9) reports the final formulation after the simplification for $\boldsymbol{x}$.

$$-\dot{\boldsymbol{M}} = \boldsymbol{A}^T\boldsymbol{M} + \boldsymbol{M}\boldsymbol{A} - \boldsymbol{M}\boldsymbol{B}\boldsymbol{R}^{-1}\boldsymbol{B}^T\boldsymbol{M} + \boldsymbol{Q} \tag{3.9}$$

Finally, once numerically integrated the solution $\boldsymbol{M}$, the optimal control is evaluated as in Equation (3.10), by substituting the linear relation in Equation (3.7) into Equation (3.4c).

$$\boldsymbol{u} = -\boldsymbol{R}^{-1}\boldsymbol{B}^T\boldsymbol{M}\boldsymbol{x} \tag{3.10}$$

The gain matrix $\boldsymbol{K}$ is then reported in Equation (3.11).

$$\boldsymbol{K} = \boldsymbol{R}^{-1}\boldsymbol{B}^T\boldsymbol{M} \tag{3.11}$$

Last but not least, the system must be fully controllable: all the components of the state vector are controllable, therefore theorem 3.1 is accomplished.

Theorem 3.1. *An LTI system is fully controllable if and only if the rank of the controllability matrix* $\mathbf{C}$ *is equal to the system order* n*.*

The criteria is accomplished if $\boldsymbol{C}$ in Equation (3.12) is full-rank. This property implies that for any initial condition $\boldsymbol{x_0}$ exists a control vector $\boldsymbol{u}$ which changes the state to another arbitrary one $\boldsymbol{x_1}$ in a finite time t_1.

$$\boldsymbol{C(A,B)} = [\boldsymbol{B},\ \boldsymbol{A}\boldsymbol{B},\ \boldsymbol{A}^2\boldsymbol{B},\ \ldots\ \boldsymbol{A}^{n-1}\boldsymbol{B}] \tag{3.12}$$

3.2.2. Implementation for ROE

The plant matrix obtained in Subsection 2.1.3 is linear and time-varying. Thus, the dynamic system in Equation (2.27) is linear as well. In Figure 3.1 the architecture of the control logic is sketched.

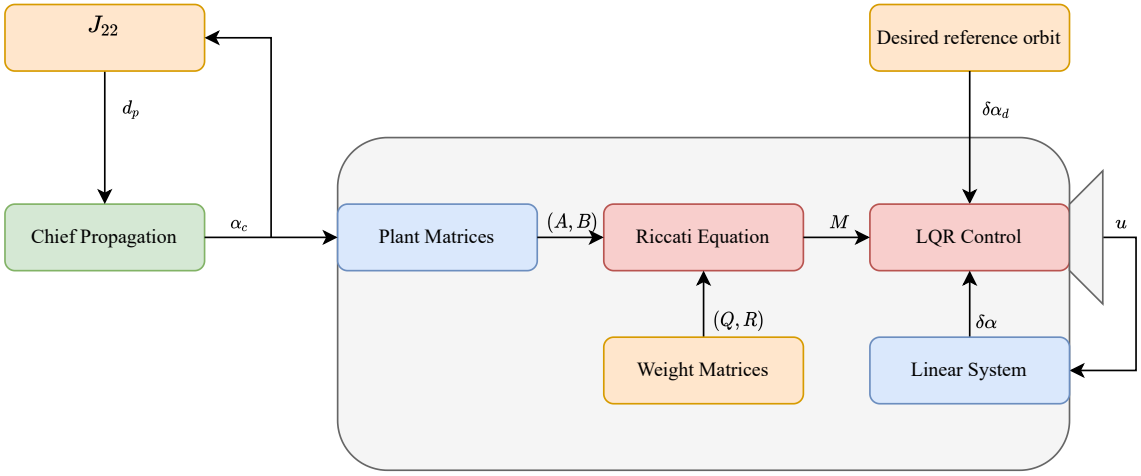

Figure 3.1: Flowchart of the simulation framework.

At each time step, the numerical propagator provides the Chief's Keplerian orbital elements $\boldsymbol{\alpha_C}$, perturbed by acceleration $\boldsymbol{d_p}$ due to J_{22}. Then the plant and control matrices ($\boldsymbol{A}$, $\boldsymbol{B}$) are updated with the result of the previous integration. Introducing the tuned weight matrixes ($\boldsymbol{Q}$, $\boldsymbol{R}$), now the differential Riccati's equation can be solved and the intermediate matrix is retrieved throughout numerical integration. Once computed $\boldsymbol{M}$, the gain matrix $\boldsymbol{K}$ can be assembled and the optimal control $\boldsymbol{u}$ calculated. This is possible by merging the desired reference relative position $\boldsymbol{\delta\alpha_d}$ and the actual one $\boldsymbol{\delta\alpha}$, obtained by closing the loop and evaluating the linear plant with the knowledge of the control actuation.

Before actually introducing the control algorithm, a check on the controllability should be performed. Recalling matrix $\boldsymbol{B}$, and keeping in mind the definition of Equation (3.12), it is possible to assure the full rank of $\boldsymbol{C}$ and therefore the controllability of the system. The matrix in Equation (3.13) is full column rank, each of the columns of the matrix is linearly independent. The controllability matrix then results as a square matrix assembled by a series of column rank matrixes multiplied by different matrixes. Therefore the nonzero determinant of $\boldsymbol{C}$ grants controllability.

$$\boldsymbol{B(\alpha_c)} = \frac{1}{n \cdot a} \begin{bmatrix} 0 & 2 & 0 \\ -2 & 0 & 0 \\ \sin(u) & 2\cos(u) & 0 \\ -\cos(u) & 2\sin(u) & 0 \\ 0 & 0 & \cos(u) \\ 0 & 0 & \sin(u) \end{bmatrix} \tag{3.13}$$

Where n is the orbit mean motion, a is its semi-major axis and $u = \omega + M$ is the argument of latitude.

3.2.3. Algorithm implementation

The main objective of the LQR is to keep Deputies' ROEs as close as possible to the desired state vector $\boldsymbol{x_d}$. The control action is the result of the difference between the linear system output and the reference condition, properly scaled by the same gain matrix: $\boldsymbol{K_d} = \boldsymbol{K}$. Equation (3.14) shows the corresponding equation. The system output $\boldsymbol{\delta y}$ exactly matches the state vector $\boldsymbol{\delta\alpha}$ made of the relative orbital elements.

$$\boldsymbol{u}(t) = \boldsymbol{K_d}\boldsymbol{\delta x_d} - \boldsymbol{K}\boldsymbol{\delta y} \tag{3.14}$$

As previously stated, information about initial and final conditions must be provided for the boundary value problem. In this case, it is convenient to reach the desired state at the last time step of the interval. Equation (3.15) shows the condition needed to obtain such a goal and its consequences.

$$\boldsymbol{M}(t = t_f) = \boldsymbol{0} \Rightarrow \boldsymbol{K}(t = t_f) = \boldsymbol{0} \Rightarrow \boldsymbol{u}(t = t_f) = \boldsymbol{0} \tag{3.15}$$

Not having clues on the intermediate matrix initial condition to start the numerical integration of the differential Riccati's equation, the selected `ode-solver` is performed backwards. $\boldsymbol{M}$ is retrieved as the only unknown, after tuning the weighing matrixes, the propagation of the Chief perturbed orbit and selecting the initial and final relative state.

In this way, the quadratic cost function to be minimised reduces to the one in Equation (3.16).

$$J(t_0) = \frac{1}{2}\int_{t_0}^{t_f} (\boldsymbol{x}^T \boldsymbol{Q}(t)\boldsymbol{x} + \boldsymbol{u}^T \boldsymbol{R}(t)\boldsymbol{u})dt \tag{3.16}$$

To visualise how the algorithm goes through the different steps algorithm 3.1 shows the path followed highlighting the most significant operations.

Algorithm 3.1 Control Algorithm

Load: `input` % Problem set-up
Propagate: `odeCart` % Chief perturbed evolution
for $t \in [t_0,\ t_f]$ **do**
  Compute $A(\alpha_c(t))$ & $B(\alpha_c(t))$ % System plant definition
end for
for $t \in [t_f,\ t_0]$ **do**
  Integrate: `odeRiccati` % Backward
  Compute $M(t)$
end for
for $t \in [t_0,\ t_f]$ **do**
  Flip: M(t) % For time coherence
  Compute $K(t)$ % Gain matrix
  Compute $u(t)$ % Optimal control
  if $u(t) < u_min$ **then**
    u(t)=0
  else if $u(t) > u_min$ **then**
    u(t)=u
  end if
  Compute $\alpha(t)$ % State update
end for
Store: $(\alpha,\ u)$ % Result report

The control algorithm determines the control action needed to solve the optimal closed-loop problem. The desired relative position is achieved at the end of the selected interval, while the fuel consumption is minimised. The given description, in which $x(t_f) - x_d = 0$, is called trajectory tracking problem. The goal is reached thanks to an asymptotic LQR design for a linear continuous system.

Setting the problem means initialising both the Chief's state and the relative initial position. Moreover, the time span has to be chosen. The initial/final time instant and the Δt, the interval of a time step. Then, having carried out a model of the gravitational perturbation, the Chief numerical propagation is performed. Once computed the natural evolution of the main spacecraft, the system is defined evaluating the plant and control matrices for each time instant.

The selection of the weighting matrices is analysed in the following section. At first, tuning is performed, then they are considered known and constant during all the controlled intervals.

Finally, the differential Riccati's equation can be integrated, starting from the end [45]. Backward integration is performed, and the null steady-state error leads to a final given value of the intermediate matrix which is defined as the "initial" condition. Before replacing M in the formulation of the gain matrix, it is necessary to re-establish the correct order of the computed matrices. In this way, the real temporal evolution is restored to the optimal control action is retrieved coherently. Finally, a check on the feasibility of the force actuation is performed. The actual technology provides very precise thrusters, however, there is a minimum amount of force that they deliver. In the end, the RTN accelerations are substituted in the plant matrix and the controlled evolution of the relative state is then carried out. The deviation error from the reference directly feed-back the control algorithm for the required next time step actuation force.

3.3. Sensitivity analysis

This analysis consists in evaluating the effects on the results induced by combinations of certain values modifications. It highlights which parameter affects the system the most and how to vary its value to better control the consequences.

By applying this strategy to the described LQ problem, it is clear that all the state variables enter in the estimation and so in the control. The evaluation of the optimal control action is goes through Equation (3.9), which minimises the cost function in Equation (3.2). This last makes explicit that the state and the control vectors actuate on the minimisation modulated by the weighting matrixes. Here is where the qualitative sensitivity analysis is performed.

By selecting different components for each of the two weighting matrices, it is possible to give more o less control effort to a specific element of the state vector. The simplest initial choice is imposing $\boldsymbol{Q}$ and $\boldsymbol{R}$ equal to the identity matrix, thus all the variables are controlled in the same manner. Then a coefficient is multiplied by $\boldsymbol{Q}$ and $\boldsymbol{R}$, the matrix related to the control vector. Broadly speaking, since the weighting matrices are constant and the same for all the Deputies, differentiating the control effort for the RTN accelerations is not effective. On the other hand, a better response is achieved by selecting different $\boldsymbol{Q}$ matrix components. Each diagonal component is not linked to all the state vectors, therefore it can be chosen the amount of effort given to each component based on the effect.

Qualitative speaking the relative mean argument of longitude $\delta\lambda$, corresponding to the 2^{nd} element, is by nature the one with the fastest variation. Then, accordingly to Subsection 3.2.1, an increment in the relative weight assures an adequate control.

3.4. Thrusters selection

The main characteristic of the control presented in this Thesis is the continuous control during orbit. Consequently, on one hand, a high onboard computational power is required and nowadays this is possible thanks to extreme miniaturisation. On the other hand, also a set of adequate thrusters is needed.

The constraints imposed by the mission are mainly related to the amount of thrust that has to be provided, the size and finally the precision and noise introduced during the operations. To maintain a tight formation, the control actuation is typically a fraction of Newtons. The physical thrusters have a lower limit for the achievable thrust and this is the first limitation to account for. Secondly, the volume of the Deputies satellite of a cluster geometry requires space management. The scientific payload, the dynamic and attitude controllers, sensors and actuators must fit, together with electric power generation and storage.

With the advent of CubeSats, the research has shifted the focus on actuators miniaturisation. Moreover, the constant progress in both electric energy generation and storage has made the implementation of electric thrusters possible. These last, lately, are one of the main fields of research, especially for relative motion. They are characterised by a higher specific impulse, therefore continuous manoeuvring is allowed [46]. A low-thrust control is more advantageous when dealing with close-proximity operations and maintains a more stable and effective control [47]. That is exactly what remote sensing missions require. Thrusters with a reduced lower limit of minimum generated force, such as cold gas o electric thrusters, are a suitable selection for this study [48, 49].

As said before, there is a physical thrust lower limit. Equation (3.17) takes into account that property and in this work the limit is considered to be $F_{min} = 10^{-7}\ N$ [49]. This value represents the lower limit of the most recent electric thruster in terms of generated thrust: $F = 0.1\ \mu N$. As shown in algorithm 3.1, if the computed optimal control in one of the RTN directions is lower, it is set to zero.

$$u(t) = \begin{cases} 0 \longmapsto if\ m \cdot\ u(t) < 10^{-7} N \\ u(t) \longmapsto if\ m \cdot\ u(t) > 10^{-7} N \end{cases} \tag{3.17}$$

Where m is the mass of the satellite, usually for Deputies CubeSats the order of magnitude is around 10^1 kg. This consideration is included to have a more realistic simulation, based on micro-Newton thrusters.

A convenient way of expressing the consumption of the propulsion thrusters is in terms of Δv. That information gives a hint on the amount of control accelerations profile on the satellite and on the total fuel budget required for keeping a mission operative during the whole lifetime. This value can be estimated numerically by integrating the total acceleration reported in Equation (3.18).

$$u_{tot}(t) = \sqrt{u_N^2(t) + u_R^2(t) + u_T^2(t)} \tag{3.18}$$

3.5. Relative position control

To avoid collisions, the relative inter-satellite distances are monitored. Once evaluated the ROEs for each satellite $\circ_k$, a transformation in relative Cartesian coordinates $(x,\ y,\ z)$ is performed according to Equation (2.14). Consequently, is immediately computed the relative position with respect to the Chief ΔR_{k-c}, as shown in Equation (3.19).

$$\Delta R_{k-c} = \sqrt{x_k^2 + y_k^2 + z_k^2} \tag{3.19}$$

A minimum inter-satellite distance constraint of $\Delta R_{min} = 7\ m$ should be imposed for all the controlled intervals to ensure safety.

On the other hand, the inter-Deputies distance constraint should be considered as well and in particular for adjacent satellites. In Equation (3.20) is reported the expression to compute the relative Deputies position ΔR_{k-c}, where j and k represent two different satellites.

$$\Delta R_{j-k} = \sqrt{(x_j - x_k)^2 + (y_j - y_k)^2 + (z_j - z_k)^2} \tag{3.20}$$

The same $\Delta R_m in = 7\ m$ is set in this case.

4 | Mission simulation results

The numerical simulation presented brings together all the formulations developed in this Thesis. The studied dynamic system embeds both the theoretical model and the control algorithm. The precise relative motion described in Chapter 2 is now part of the overall dynamics. It has been merged with the implemented LQR method for optimal formation-keeping.

The ROEs allow expressing the whole model in an analytical framework, only requiring the updating of the Chief's Keplerian orbital elements. The control matrix computed plays a key role in linking the RTN acceleration with the relative motion. In this way, the closed-loop control logic presented in Chapter 3 is included. Through the control actions, the state is retrieved and it can feedback to the system that with this information actualises the optimal control.

4.1. Overview of the mission scenario

In this Thesis, a test case of a remote sensing mission is studied. A cluster formation of seven satellites, one Chief and six Deputies, is propagated during a time span of $T = 10\ days$. The interval has been selected to appreciate the natural evolution and the corresponding control without accounting for station-keeping.

The central spacecraft orbits in GEO and its initial conditions are reported in Tables 4.1 and 4.2. The Cartesian coordinates are reported in the Earth MJ2000Eq reference system and they represent geostationary orbit at the Greenwich meridian. The Keplerian elements are computed with GMAT, which does not suffer from singularities with these magnitudes for e and i. The chosen set of initial conditions does not present singularities neither for the implemented formulation while describing a suitable desired position above central Europe.

Parameter	Value	Unit
X	-36372.671	km
Y	21328.079	km
Z	60.986	km
V_X	-1.555	km/s
V_Y	-2.652	km/s
V_Z	$2.453 \cdot 10^{-3}$	km/s

Table 4.1: Cartesian Initial condition.

Parameter	Value	Unit
a	42166.279	km
e	$3.746 \cdot 10^{-5}$	-
i	$9.464 \cdot 10^{-2}$	deg
Ω	88.494	deg
ω	61.120	deg
θ	0	deg

Table 4.2: Keplerian Initial condition.

Around the main satellite, the six Deputies are placed in the geometry shown in Figure 4.1, which represents the initial condition of the formation. The configuration for the seven micro-satellites is based on a regular hexagon inscribed in a circumference of ten metres radius. Working on a small scale is not a limit, with the tuning of the implemented control, it can be applied to larger variants. The figure is a plot in the RTN frame and the origin coincides with the Chief.

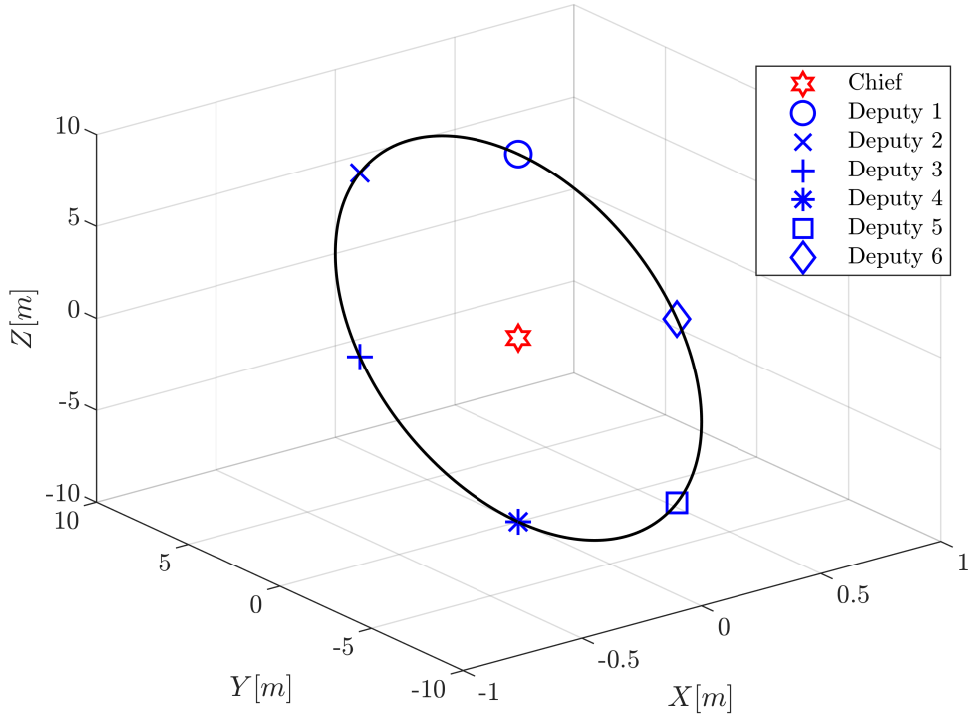

Figure 4.1: Initial cluster formation.

The presented tight formation should be kept as rigid as possible. The retrieved initial Relative Orbital elements, reported in Table 4.3, are chosen to be the desired state as well. In this way, the computed values are included in the formulation both as initial conditions for the ROEs evolution and as the reference target configuration.

Deputy	δa **[m]**	$\delta\lambda$ **[m]**	δe_x **[m]**	δe_y **[m]**	δi_x **[m]**	δi_y **[m]**
1	0.0158	0.0149	-0.2418	0.1349	4.7835	-12.0342
2	8.7632	7.4893	-4.6274	7.5477	0.4045	-9.6198
3	8.7343	7.4980	-4.5452	7.4864	-8.3526	-4.7904
4	-0.0421	0.0303	-0.0779	0.0115	-12.7307	-2.3754
5	-8.7895	-7.4442	4.3075	-7.4018	-8.3520	-4.7908
6	-8.7606	-7.4522	4.2261	-7.3398	0.4051	-9.6201

Table 4.3: Initial Relative Orbital Elements.

All the following figures and tables presenting ROEs evolution are scaled for the Chief's semi-major axis for better readability. The state vector is multiplied by the semi-major axis of the Chief satellite, as in Equation (4.1), to restore dimension and then is expressed in metres to have a better visual representation.

$$\delta\alpha_{plot} = 10^3 \cdot a_c \cdot \delta\alpha \tag{4.1}$$

4.2. Validation

To validate the model presented in Chapter 3, all the presented formulations are compared with a high fidelity simulator. The *General Mission Analysis Tool* (GMAT) is an open-source software developed by NASA to propagate any spacecraft given the environmental and initial conditions [50]. For Thesis purposes, the natural dynamics have been perturbed only by the gravitational potential described by *JGM2*. The model is truncated a the second degree and order, to introduce the J_{22} effect.

4.2.1. Chief propagation

First of all, the validation of the Chief propagator is performed. The chosen Cartesian equations must provide a feasible estimation of the real evolution of the satellite. Figure 4.2 shows the comparison between the Cartesian propagation implemented in this work and the GMAT tool. The results show a good match between the two models.

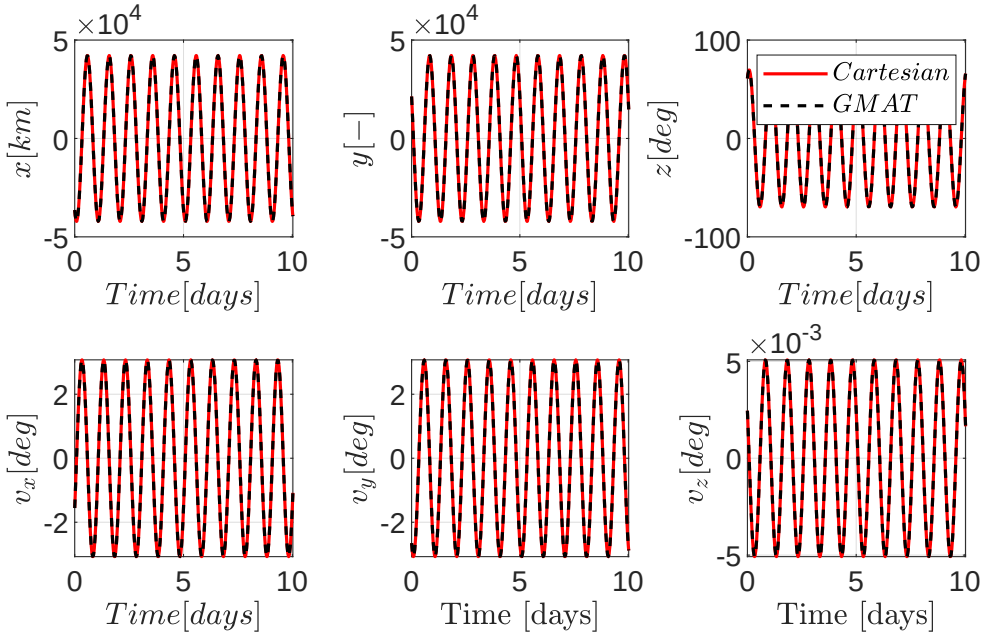

Figure 4.2: Propagation comparison between Cartesian equations and GMAT.

To better understand the absolute error between the propagators, the norm of both Cartesian position and velocity are computed. The result in Figure 4.3 indicates that the difference is just above respectively 100 m and 4 m/s, during the selected period.

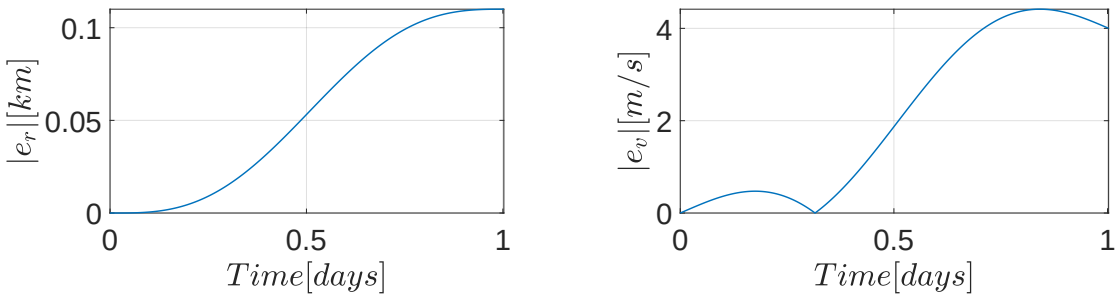

(a) Cartesian position.

(b) Cartesian velocity.

Figure 4.3: Absolute error.

4.2.2. Control tuning

Exploiting a shorter period, it is possible to run multiple simulations to tune the weighting matrices and to assure the convergence of the control. Figures 4.4, 4.6 and 4.7 show Relative Orbital Elements' controlled evolution of one Deputy for about 0.1 *orbital periods*. The differences in the plots are due to the change in the weighting matrices: each figure corresponds to one of the three steps described in Section 3.3.

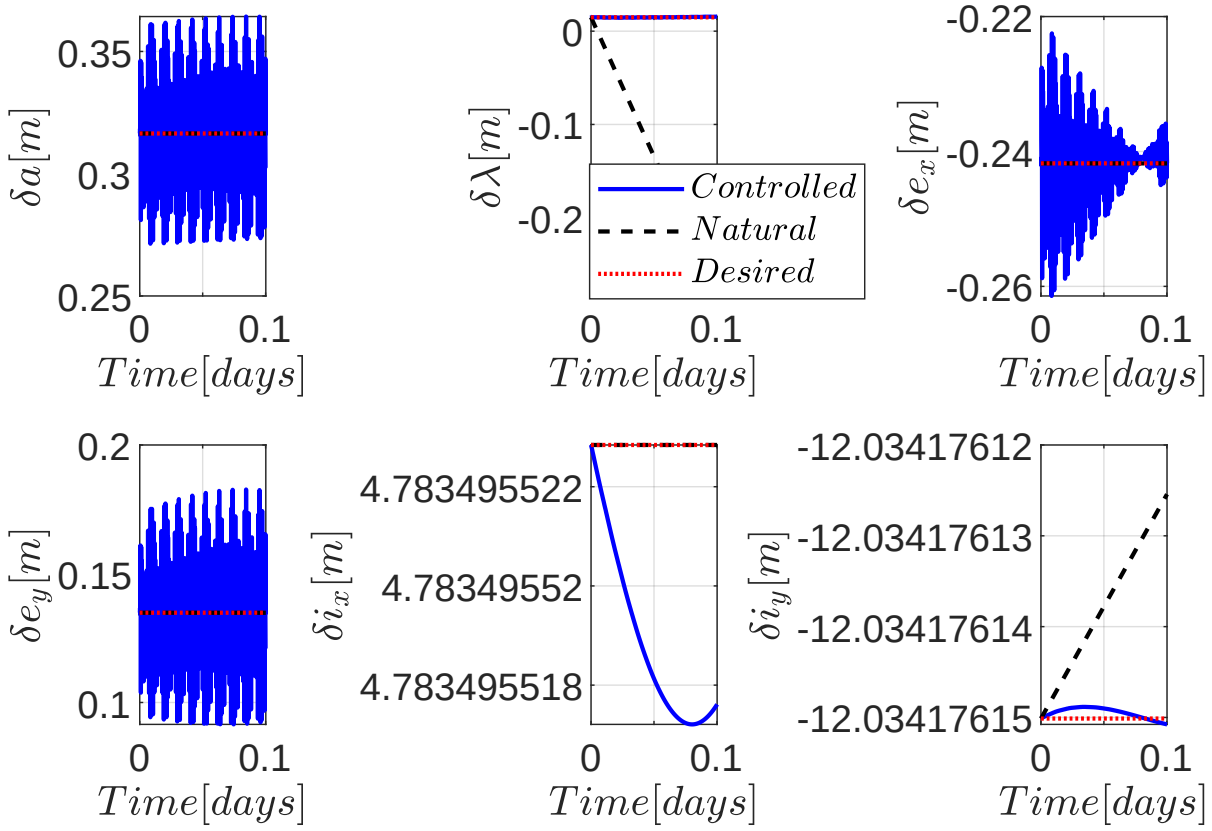

Figure 4.4: Control with identity weighting matrices.

At first, the gain matrix $\boldsymbol{Q}$ and $\boldsymbol{R}$ are identity matrices of dimensions 6 and 3, respectively. The control converges but, as visible in Figure 4.5, the steady-state error is limited, but it is above the scientific requirements ($\approx 1\ cm$) for most of the states. Figure 4.4 shows significant oscillations, especially for the first element.

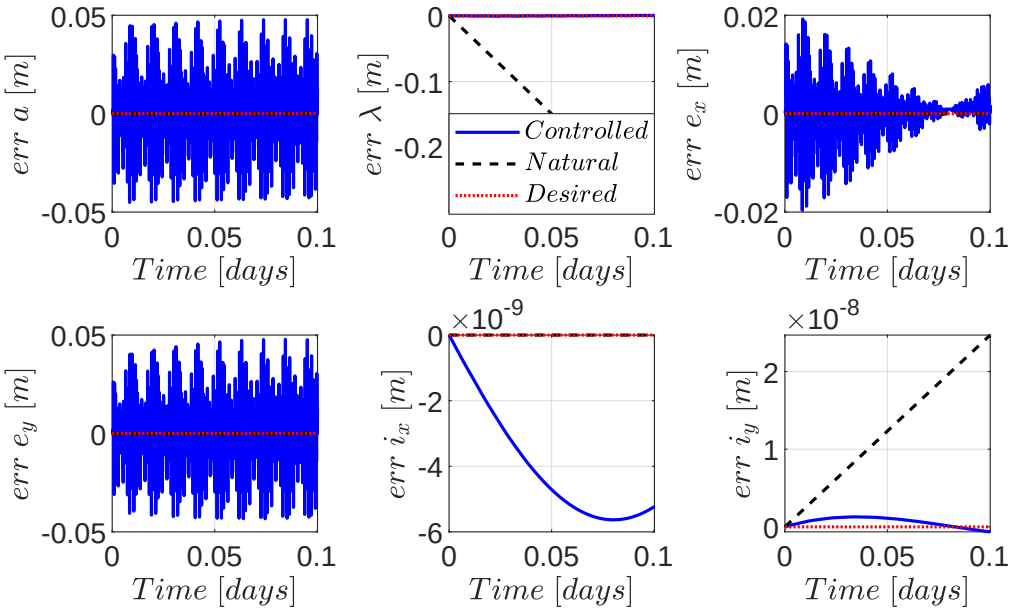

Figure 4.5: Steady State Error with identity weighting matrices.

Fluctuations of 50 *cm* correspond to the difference in terms of the semi-major axis which is not acceptable for implementing interferometry. The discrepancy is visible also for eccentricity components. Performing continuous control, all the state components are affected, even the ones with slow or constant variations. This is an inevitable side effect, however, it can be mitigated and it is acceptable as long as the variations are inside the prescribed range.

In the second step, a scaling parameter $\rho = 10^{-3}$ is multiplied by both matrices separately.

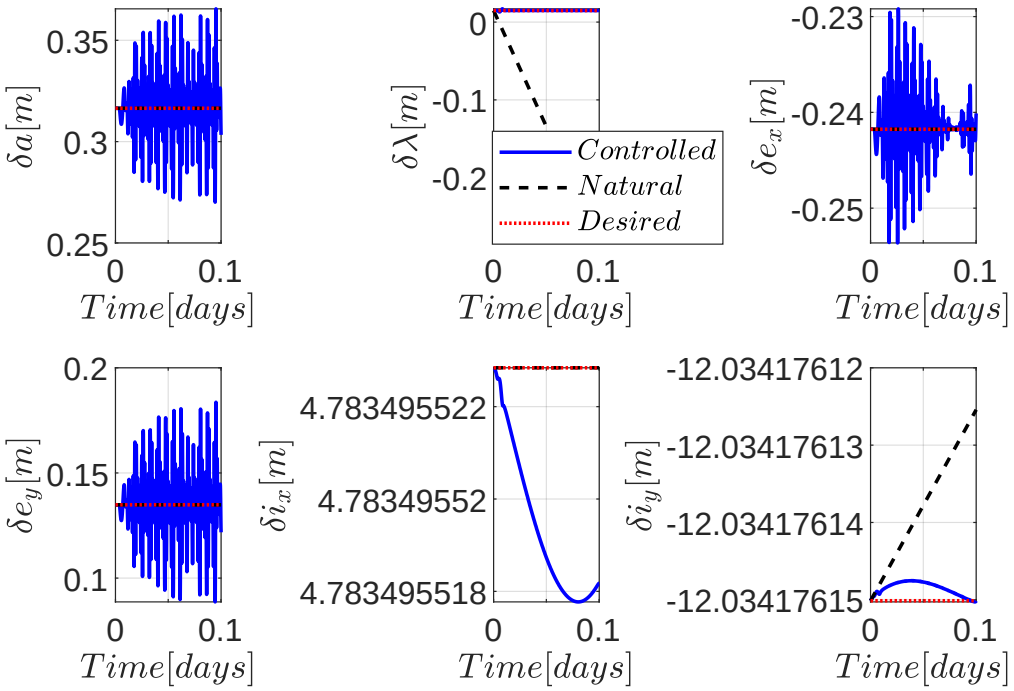

(a) Scaled $\boldsymbol{Q}$.

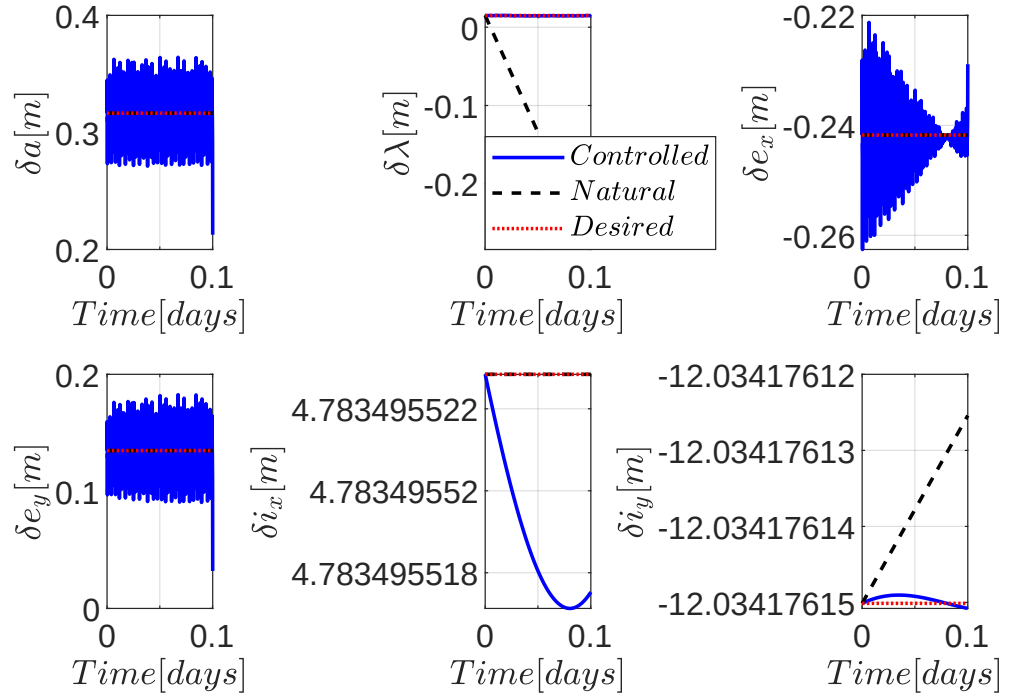

(b) Scaled $\boldsymbol{R}$.

Figure 4.6: Control with scaled weighting matrices.

On one hand, the scaled matrix $\boldsymbol{R}$ does not seem to give any variation to the state vector evaluated without scaling and the result is close to the one obtained in Figure 4.4. The behaviour of the elements of the state vector appears to worsen by tuning the matrix corresponding to the accelerations. Moreover, the relation between the control action and its effect on the state vector is not straightforward. On the other hand, modifying the matrix $\boldsymbol{Q}$ provides an improvement in the results of the control strategy. In Figure 4.6a, δa, δe_x and δe_y have experienced a positive effect, different from the behaviour in Figure 4.6b. In the following, the analysis of the gain matrices focuses only on the shifted values of the matrix $\boldsymbol{Q}$. The benefit for δa is visible but still not compliant with the scientific instrumentation. By modifying the diagonal elements of Q, the consequences are reflected directly in the state. That is the logic according to which the values have been selected.

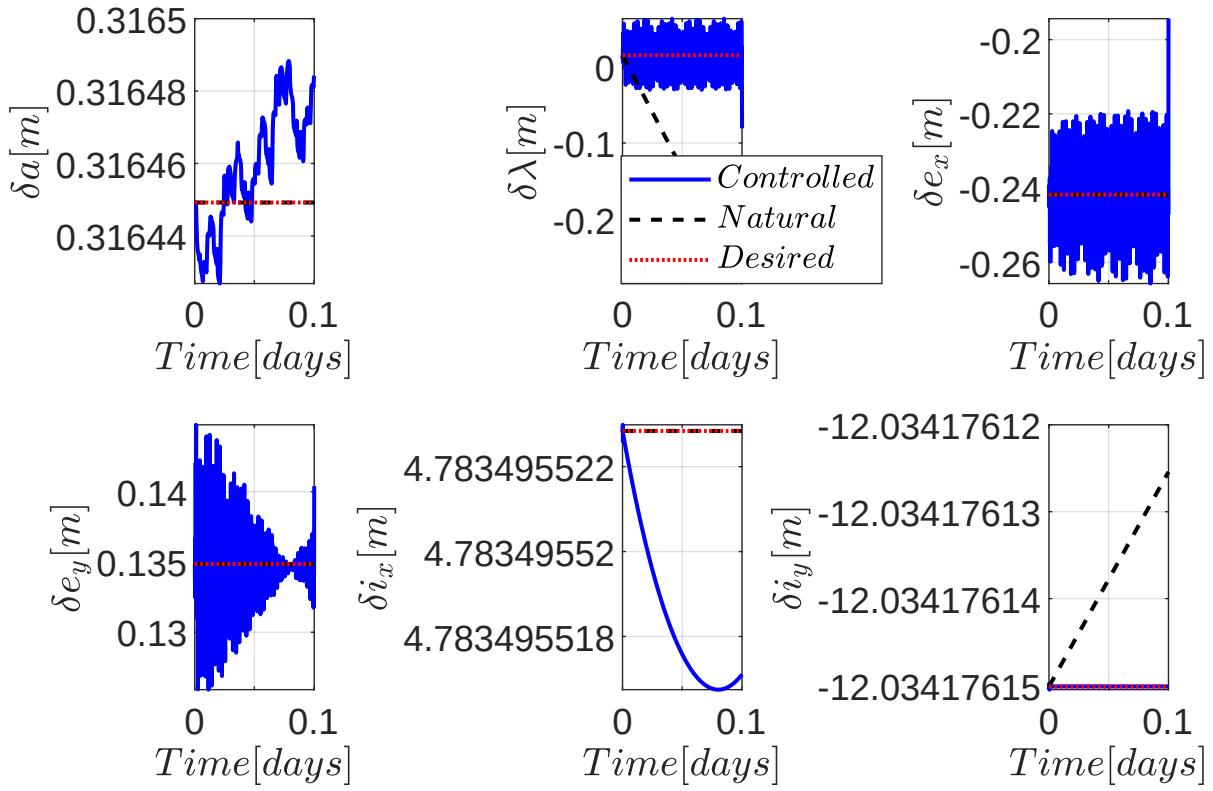

Figure 4.7: Control with tuned weighting matrix.

Analysing the effect of each diagonal component of the weighting matrix $\boldsymbol{Q}$, important relations have been identified. The fast variation related to $\delta\lambda$ must be dealt with. Increasing the value of the second diagonal element $\boldsymbol{Q}(2,2)$, the control is adapted to the problem and the system response is improved. The more weight is put there, the better the result gets. Finally, after some trial and error, the values of matrices $\boldsymbol{Q}$ and $\boldsymbol{R}$ have been selected and reported in Equations (4.2) and (4.3).

By reducing the third and the fourth element, the ones related to the eccentricity, the control of that specific Keplerian element is decreased. This operation seems to improve the control of the other state components. No further modifications are implemented on the almost constant ROEs δa and δi_x. This selection is the one used to retrieve the plots in Figure 4.7 and for the following sections. It seems to provide better results in terms of the control of the ROEs components.

$$\boldsymbol{Q} = 10^{-3} \begin{bmatrix} 1 & 0 & 0 & 0 & 0 & 0 \\ 0 & 1000 & 0 & 0 & 0 & 0 \\ 0 & 0 & 0.1 & 0 & 0 & 0 \\ 0 & 0 & 0 & 0.1 & 0 & 0 \\ 0 & 0 & 0 & 0 & 1 & 0 \\ 0 & 0 & 0 & 0 & 0 & 1000 \end{bmatrix} \tag{4.2}$$

$$\boldsymbol{R} = \begin{bmatrix} 1 & 0 & 0 \\ 0 & 1 & 0 \\ 0 & 0 & 1 \end{bmatrix} \tag{4.3}$$

4.3. Simulation results for formation maintenance

In this section, the control logic developed in this thesis, based on the gain matrices $\boldsymbol{Q}$ and $\boldsymbol{R}$ shown in Subsection 4.2.2, is applied to the formation maintenance of the test case scenario described in Section 4.1. The dynamics of the six Deputies are propagated for ten days with the tuned control algorithm. The same pattern is adopted for the presentation of the results of all the spacecraft.

4.3.1. Controlled dynamics

First of all, the ROEs evolutions are portrayed. In the same figure, the controlled ROE (in blue), their natural evolution (in dashed black) and the desired state (in dotted red) are plotted. All the images are visualised in metres according to Equation (4.1).

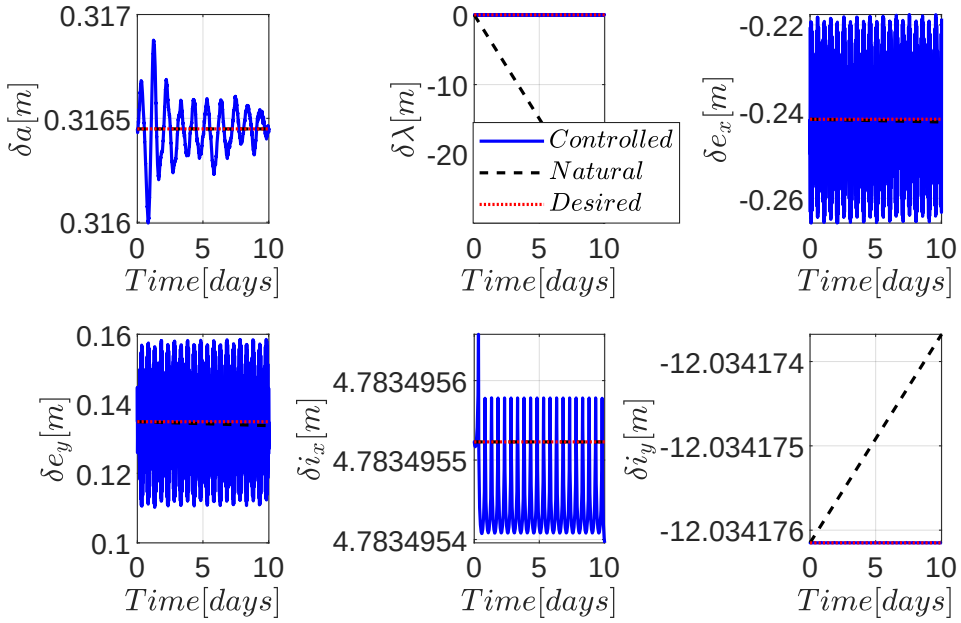

Figure 4.8: ROE controlled evolution of Deputy 1.

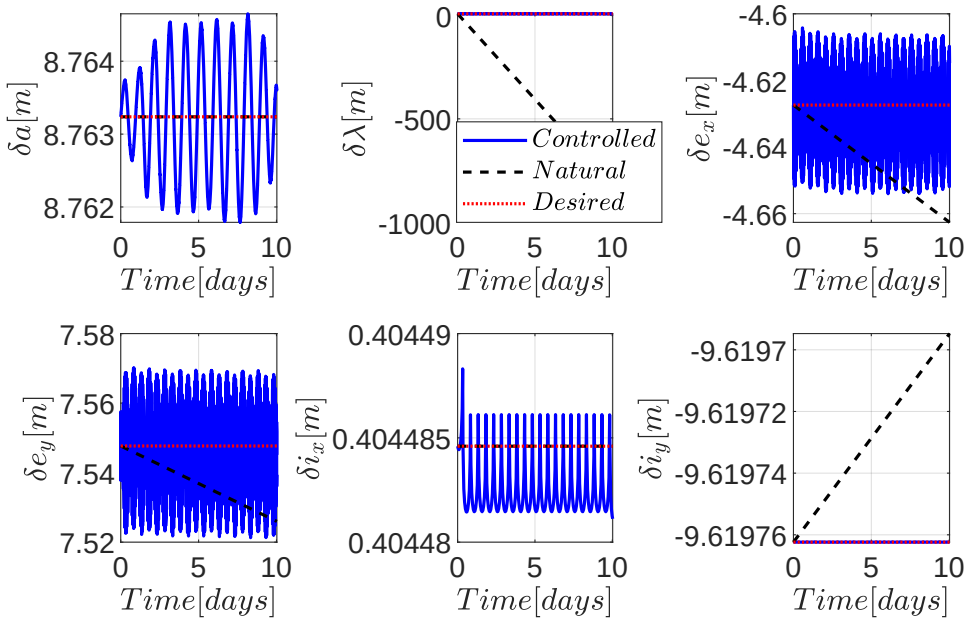

Figure 4.9: ROE controlled evolution of Deputy 2.

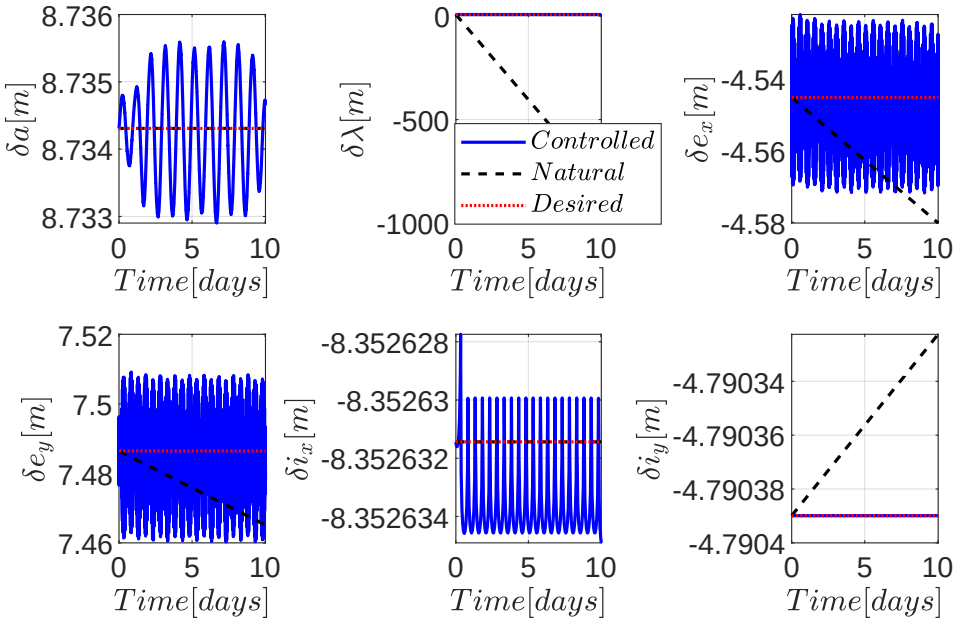

Figure 4.10: ROE controlled evolution of Deputy 3.

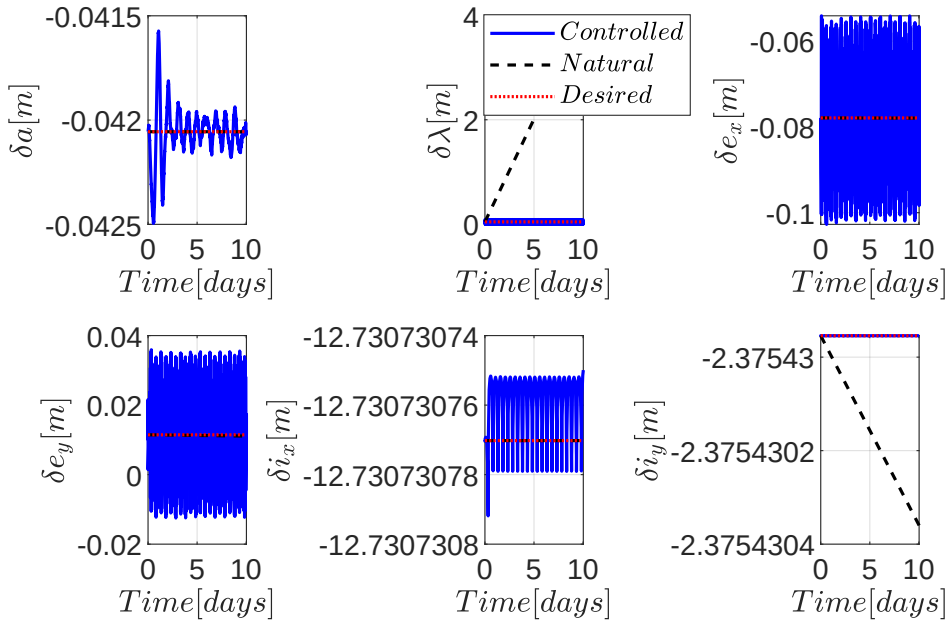

Figure 4.11: ROE controlled evolution of Deputy 4.

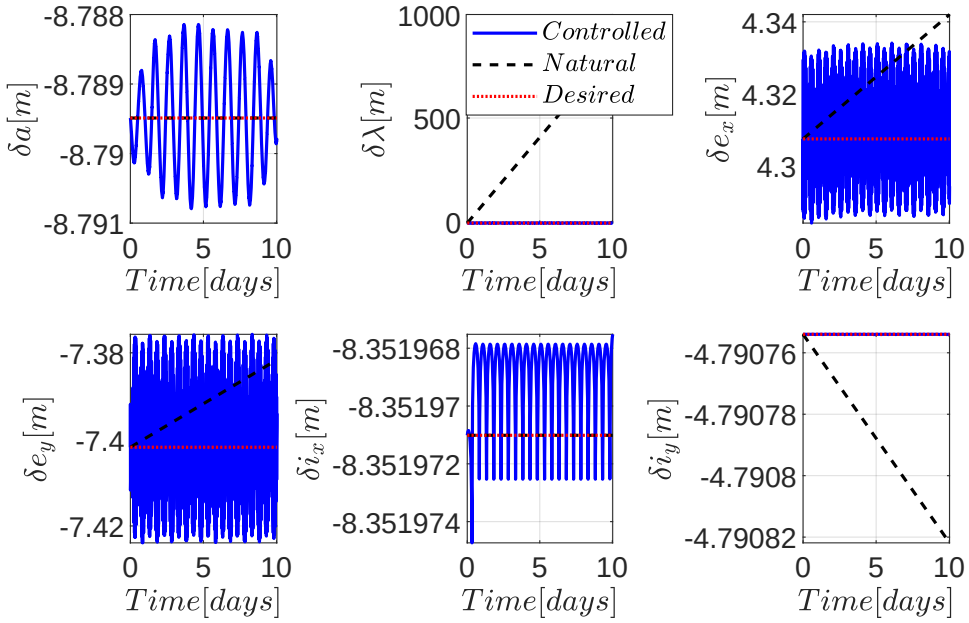

Figure 4.12: ROE controlled evolution of Deputy 5.

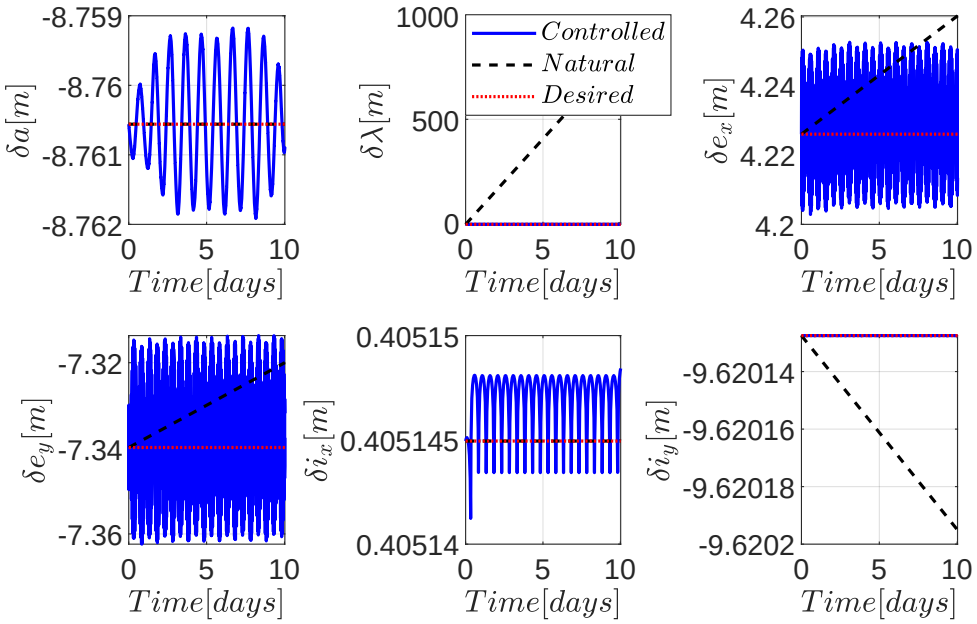

Figure 4.13: ROE controlled evolution of Deputy 6.

As expected, all the relative orbital elements oscillate around the prescribed reference value. Even when the variations seem to be significant, it is important to consider the scale of the axis. The parameters δe_x and δe_y which appear to be the ones with the less accurate control, present a maximum oscillation of about 20 cm. Transforming this difference in dimensionless ROEs terms, it corresponds to a variation of 10^{-10} around the desired value which is of the order of 10^{-7}. The element linked with the semi-major axis δa, the one with the most direct physical meaning, is affected by an error smaller than two millimetres from the desired condition. This situation is valid also for the satellites for which the control is less precise. The fast variation of the mean argument $\delta\lambda$ of longitude is completely counteracted by the optimal control. The geodetic effect seems to not affect δi_x and δi_y their natural evolution is almost constant, which is consistent with the equatorial nature of the orbit.

The ROEs in Figures 4.8 and 4.11 are characterised by similar behaviour one to another. The perturbing geodetic effect depends on the longitude, therefore Deputies 1 and 4 are affected by similar accelerations, effectively counteracted by the control. This pattern is also present for the couple 2-3 in Figures 4.9 and 4.10 and 5-6 in Figures 4.12 and 4.13. The accuracy is slightly less performing for these last two couple due to the tuning held on Deputy 1.

4.3.2. Deviation from the desired position

Moreover, it is reported the difference between the actual position in the RTN frame and the nominal one. The mapping from ROEs to the magnitude of the Cartesian vector is done following Equation (2.14).

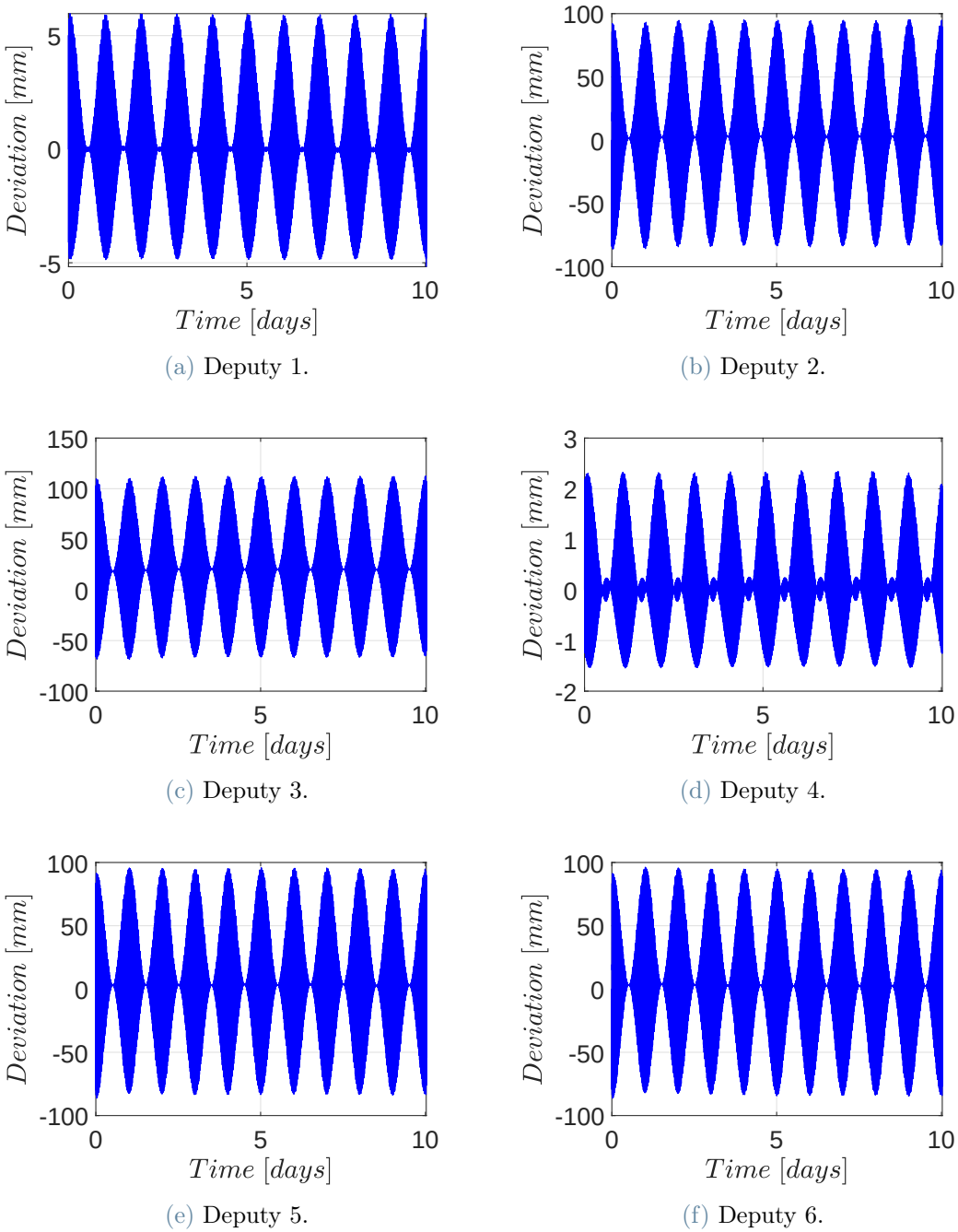

(a) Deputy 1.

(b) Deputy 2.

(c) Deputy 3.

(d) Deputy 4.

(e) Deputy 5.

(f) Deputy 6.

Figure 4.14: Relative Cartesian deviations from relative positions.

What seen in Subsection 4.3.1 is then reflected here. Figures 4.14a and 4.14d highlight the better accuracy retrieved for the first and fourth Deputy. In any case, noticing the scale, even for the other satellites, the deviation from the mean null value is bounded around one centimetre. The control succeeds in keeping the deputies close to their desired relative position.

Then, the analysis of the graphics is resumed in a table that reports the initial/desired condition, the final achieved magnitude of the relative position and the deviation from the reference position. The dispersion statistical index σ is evaluated as in Equation (4.4) and it represents the dispersion coefficient.

$$\sigma = \sqrt{\frac{1}{N}\sum_{i=1}^{N}(x_i - x_d)} \tag{4.4}$$

Deputy	Initial/Desired Position [m]	Final Position [m]	Dispersion [mm]
1	10	10.017	3.904
2	10	10.064	57.869
3	10	10.151	63.263
4	10	10.002	4.067
5	10	10.049	61.153
6	10	10.019	61.950

Table 4.4: Resume of the deviations from desired state.

Having a look at the values in Table 4.4, it can be noticed that the dispersion between Deputies laying in an opposite position of the formation (1-4; 2-5; 3-6) are related one to another. That is explained by remembering that the tuning of the control algorithm has been performed only on the first Deputy and the perturbation due to J_{22} has the same effect on spacecraft considered at the same longitude. Nevertheless, the control is effective and below the required precision needed from the instrumentation. The relative inter-satellite distance is maintained close to the desired one, after the reverse mapping from ROEs to Hill frame and retrieving the relative Cartesian coordinates. The mean value of each deviation reflects the dispersion coefficient. Deputy 3 differs for less than 15 cm and it is the worst case. Furthermore, those satellites over whom the control has been tuned do not exceed a few millimetres variations.

4.3.3. Control effort

The control action profile is also reported. The vector u representing the control accelerations is stored and then plotted in m/s^2. Their reference frame is the Hill frame, therefore each of the three components is aligned with the radial, tangential and normal direction concerning the Chief position. The total magnitude of the acceleration, retrieved from Equation (3.18) is then computed and tabled together with the corresponding Δv.

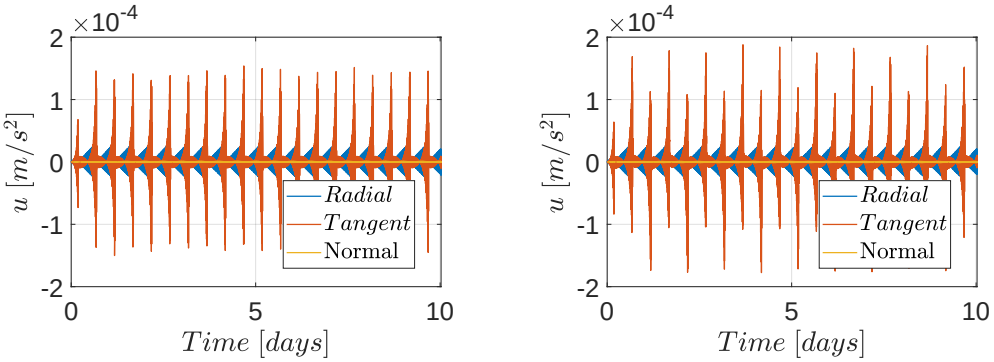

(a) Deputy 1.

(b) Deputy 2.

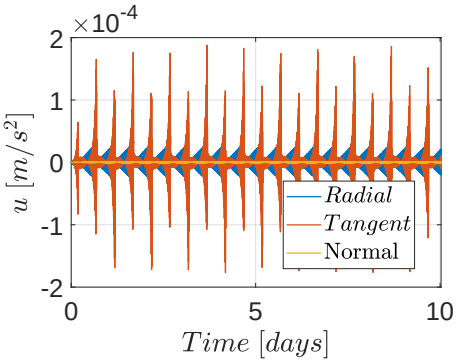

(c) Deputy 3.

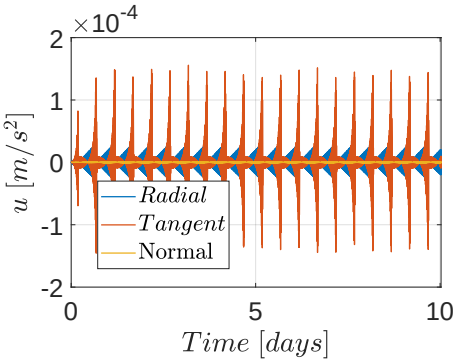

(d) Deputy 4.

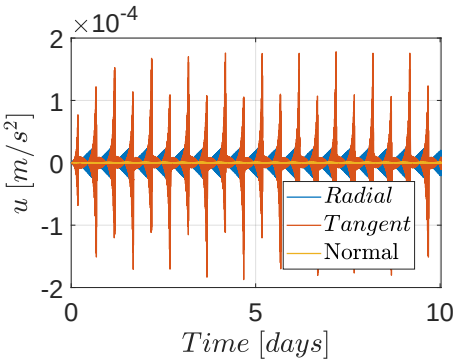

(e) Deputy 5.

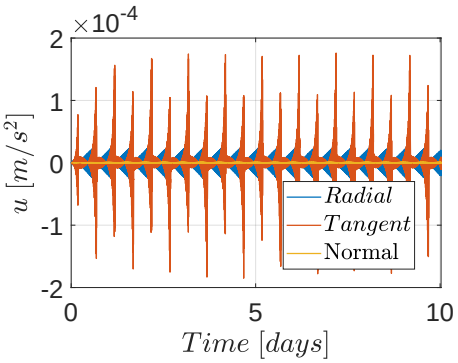

(f) Deputy 6.

Figure 4.15: Control action in Hill frame.

The components of the accelerations plotted in Figure 4.15 graphically show in which direction the Deputies must be corrected the most. To overcome the displacements especially in δa and $\delta\lambda$, the control effort is concentrated in the tangential direction. The optimal control evaluates that, controlling mainly that direction, the corresponding Δv and consequently the thrust are minimised.

Some spikes are visible analysing the figures. This behaviour can be caused by the limitation in thrusters lower limit in thrust generation. When the calculated control action is below that threshold, the algorithm does not perform any actuation in the seek of realism. An overshoot might be observed when the control is resumed.

In this section the total Δv_{tot} required from each satellite to perform the optimal control evaluated previously is computed. The built-in Matlab function `trapz` computes the approximate integral of the total acceleration u_{tot}, as in Equation (3.18), via the trapezoidal method for the whole ten days interval. The results are reported in Table 4.5 for each Deputies.

Deputy	$\Delta v_{tot}\ [m/s]$
1	6.866
2	7.776
3	7.772
4	6.858
5	7.703
6	7.710

Table 4.5: Total Δv during ten days.

The required delta velocity is almost the same for all the spacecraft. Again, the selected tuning favours Deputies 1 and 4. The corresponding thrust linked to these Δvs is computed according to the second Newton's law: $T = m \cdot u$, where the mass is set to $m = 10\ kg$. As shown in Figure 4.16, thrusters must be able to provide fractions of Newtons, micro-thrusters (μN) are required.

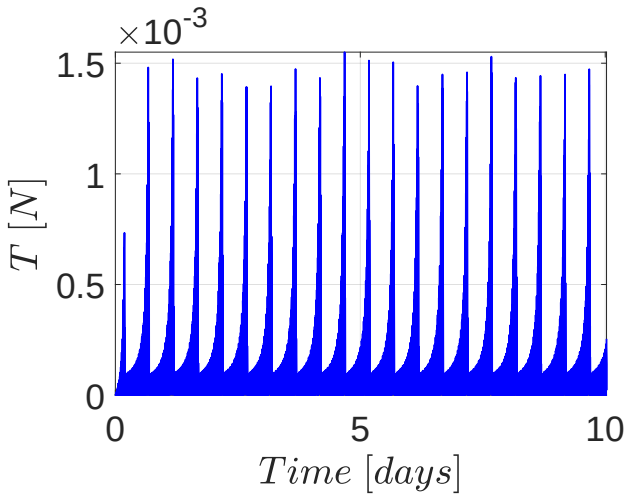

Figure 4.16: Thrust level.

4.3.4. Inter-satellite distances

In the end, following the steps described in Section 3.5, the final check is graphically reported. The distance evolution of each satellite, with reference to the Chief and its adjacent Deputies is plotted. The minimum range of 7 m is shown (in dashed black) together with the inter-satellite distance (in blue) and the desired one (in dotted red).

The analysed parameter is ΔR, as in Equation (4.5). The expression is referred to Hill's relative coordinates $(x,\ y,\ z)$, it is the same for any pair of spacecraft $m-n$. Consistently with the definition of the reference frame, the chief position corresponds to the origin.

$$\Delta R_{m-n} = \sqrt{(x_m - x_n)^2 + (y_m - y_n)^2 + (z_m - z_n)^2} \tag{4.5}$$

At first, the distances relative to the Chief are plotted during the interval. The gain matrices are tuned on the first Deputy and this is mirrored in Figure 4.17. The other satellites experience wider oscillation, always granting the precision required by the technical instrumentation.

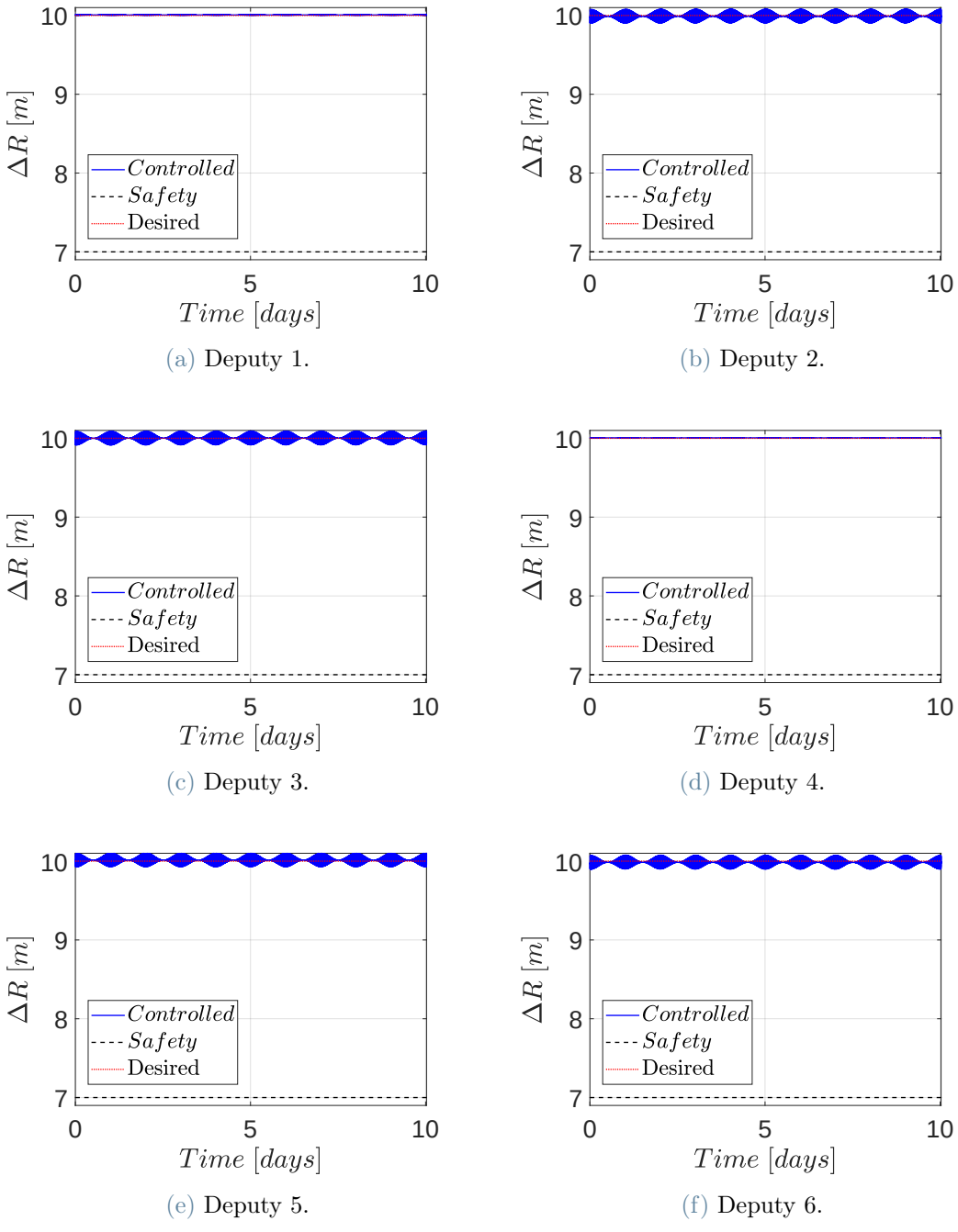

(a) Deputy 1.

(b) Deputy 2.

(c) Deputy 3.

(d) Deputy 4.

(e) Deputy 5.

(f) Deputy 6.

Figure 4.17: Satellites distances from Chief.

In the same way, Figure 4.18 reports the relative position between adjacent satellites. The risk of spacecraft getting too close to one another is fully prevented during the whole mission lifetime. The amplitude oscillations around the nominal distances depends on the Deputies couple. Two satellites sharing the same longitude, as happens for the couples 2-3 and 5-6, are affected by almost identical perturbations. Therefore, the unique control

logic acts in the same measure for both the spacecraft.

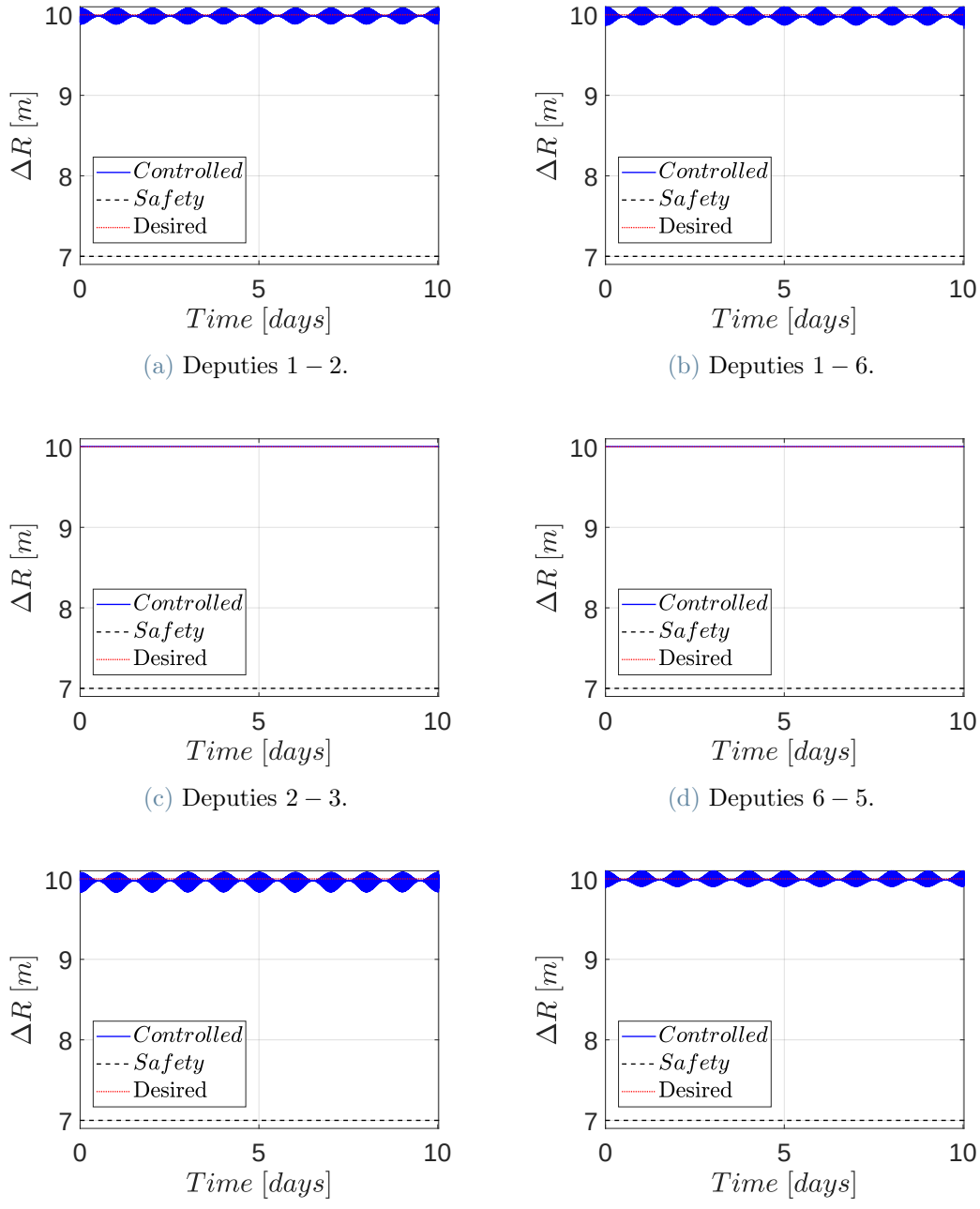

(a) Deputies $1-2$.

(b) Deputies $1-6$.

(c) Deputies $2-3$.

(d) Deputies $6-5$.

(e) Deputies $3-4$.

(f) Deputies $5-4$.

Figure 4.18: Inter-satellites distances.

This subsection highlights, through figures, the compliance of the safety distance constraint. The relative position of each Deputy does not violate the mission requirement for avoiding collisions at any moment.

5 | Conclusions and future developments

The implementation of interferometry for space remote sensing missions is arousing interest in the scientific community. The achievable spatial resolution leads the way to a growing number of studies and researches aiming at proceeding in the technology readiness levels. The objective of this research is in that direction, with a particular focus on the Geostationary orbit applications. At these altitudes, if proper control is implemented, the observed region remains the same and the temporal resolution can be improved. Therefore, enhanced natural and relative dynamics are required.

5.1. Conclusions and lessons learnt

A remote sensing mission in Geosynchronous equatorial orbit exploiting a distributed payload has been analysed. The simulation of rigid and tight formation has been propagated for ten days. In Chapter 2 is developed an analytical framework that includes the effect of Geodetic perturbations up to the second order. The implementation of Mean Relative Orbital Elements has resulted effectively for Formation-Flying applications. Exploiting that formulation, the dynamic system is linearized and efficiently numerically propagated. The disturbing acceleration due to J_{22} has been introduced in the State Transition Matrix by computing the partial derivatives of the Chief's orbital elements with respect to the Relative Orbital Elements. The innovative natural model obtained has been successfully validated with the NASA solver GMAT. For Formation-keeping purposes, in Chapter 3 an optimal control logic is analysed. A continuous formulation with low-thrust feedback control has been selected. The problem is formulated as Linear Quadratic and the minimization of the control effort is obtained by solving the Differential Riccati Equation. The Linear Quadratic Regulator is tuned after performing a sensitivity analysis, the result assures a control accuracy in the centimetres order. Finally, in Chapter 4 the simulation results are presented where the main mission constraints have been considered, inter-satellite distance for instance.

The main feature of the proposed model is linearity, consequently, a robust and accurate family of controllers has been implemented. Moreover, the selected set of parameters allows keeping a link between the relative motion and its visual representation. In terms of practical findings, despite the ideal nature of the implemented actuators, it has been proved that low thrust continuous control is a feasible choice for this kind of mission, laying the foundations for future space tests.

5.2. Limitation of the work

This study is subject to limitations that can affect the work. The presented analysis is developed considering the controlled state as exactly known at each time step for each deputy. During the in-space operations, the relative positions are retrieved by sensors, which consequently introduce noise. Even if the promising results, obtained thanks to the described model, might mitigate the disturbance with the implementation of a Kalman filter, there is no evidence of how the system would react. The same consideration applies to thrusters, the calculated control action will not coincide exactly with the one provided by the actuators. Significant biases might be introduced, considering the level of precision required by the scientific mission. The lack of a thruster model does not allow to grant that the centimetre accuracy is maintained regardless of the noise introduced.

5.3. Further studies and applications

The future developments of this work should go in the direction of designing a real mission for interferometry in higher orbits. Starting from the dynamic model, other perturbations due to third bodies, Solar Radiation Pressure and higher Geodetic orders might be taken into account. The matricial formulations allow superposing the effects, maintaining all the resulting benefits. An analysis of satellites' attitude dynamics and control should also be implemented. The orientation of the satellites is a crucial feature not only for the scientific payload but also for the orbital dynamics (perturbations due to Sun depends on the cross area) and for the power budget as well.

Once this technology will comply with the "flight qualified" requirements, then a wide range of new applications will be available. Mention one of them, Single-pass Synthetic Aperture Radiometry tomography. Nowadays, multiple passages or multiple satellites are needed to elaborate tomography imaging. The development of these kinds of missions in geostationary orbit will improve the actual surveillance and data monitoring capabilities for a precise area on the globe.

Finally, before concluding this chapter, a small discussion about the deputies' attitude must be included. Along with this document, the spacecraft's body axes are assumed to be always coincident with the Radial-Tangential-Normal frame, and the thrusters are aligned with these directions. This, however, might not be true in general, as the control accelerations can also influence the spacecraft's attitude, creating a misalignment between the directions of the thrusters and the selected frame. Because the required control actions are all computed there, two different options could be considered to account for this possible misalignment. The first case is to rotate the required accelerations from the Radial-Tangential-Normal frame to the spacecraft's body-fixed frame, to compute the actual inputs that should be sent to the actuators. To implement this rotation, the actual attitude of the spacecraft must be known. The second option is implementing an attitude control algorithm, which can ensure that the body-fixed axis and the reference frame are aligned at each time instant. With either of these two options, the model predictive control algorithms could be used in more realistic scenarios, including the spacecraft's attitude.

A | Orbital elements partial derivatives

In this appendix, the equations describing the secular and periodical variation of the Keplerian orbital elements are reported. The initial total derivatives are described by Vallado and McClain in [30].

Secular variation of the Keplerian elements

Semi major axis, a

$$\dot{a} = 0 \tag{A.1}$$

Eccentricity, e

$$e = \sqrt{e_x^2 + e_y^2} \tag{A.2}$$

$$\dot{e} = 0 \tag{A.3}$$

Inclination

$$\dot{i} = 0 \tag{A.4}$$

Right Ascension of the Ascending Node

$$\dot{\Omega} = -\frac{3}{2} J_2 \left(\frac{R_\oplus}{a} \right)^2 \frac{1}{(1-e^2)^2} \cos(i) \tag{A.5}$$

Argument of the perigee

$$\dot{\omega} = \frac{3}{4} J_2 \left(\frac{R_\oplus}{a}\right)^2 \frac{1}{\left(1-e^2\right)^2} \left(5\cos\left(i\right)^2 - 1\right) \tag{A.6}$$

Mean Anomaly

$$\dot{M} = 1 + \frac{3}{4} J_2 \left(\frac{R_\oplus}{a}\right)^2 \frac{1}{\left(1-e^2\right)^2} \sqrt{1-e^2} \left(3\cos\left(i\right)^2 - 1\right) \tag{A.7}$$

Periodic variation of the Keplerian elements

$$\dot{a}_{22} = 0 \tag{A.8}$$

$$\dot{e}_{22} = 0 \tag{A.9}$$

$$\dot{i}_{22} = 0 \tag{A.10}$$

$$\dot{\Omega}_{22} = J_{22} \left(\frac{R_\oplus}{a}\right)^4 \frac{1}{\left(1-e^2\right)^4} \cos\left(i\right) \left(\left(\frac{-45}{8} + \frac{3}{4}e^2 + \frac{9}{32}e^4\right) + \tag{A.11}$$

$$+ \left(\frac{57}{8} - \frac{69}{32}e^2 + \frac{27}{64}e^4\right) \sin\left(i\right)^2\right)$$

(A.12)

$$\dot{\omega}_{22} = J_{22} \left(\frac{R_\oplus}{a}\right)^4 \frac{1}{\left(1-e^2\right)^4} \left(\left(\frac{27}{2} - \frac{15}{16}e^2 - \frac{9}{16}e^4\right) + \tag{A.13}$$

$$+ \left(\frac{507}{16} + \frac{171}{32}e^2 + \frac{99}{64}e^4\right) \sin\left(i\right)^2 + \left(\frac{1185}{64} - \frac{675}{128}e^2 - \frac{135}{128}e^4\right) \sin\left(i\right)^4\right)$$

$$\dot{M}_{22} = 1 - J_{22} \left(\frac{R_\oplus}{a}\right)^4 \frac{1}{\left(1-e^2\right)^4} \sqrt{1-e^2} \left(\frac{5}{64}\right) \left(2-e^2\right) \sin\left(i\right) \tag{A.14}$$

Auxiliary function

$$g = \dot{\omega} + \dot{\Omega}\cos(i) + \dot{M} = \tag{A.15}$$
$$= \frac{3}{4}J_2\left(\frac{R_\oplus}{a}\right)^2 \frac{1}{(1-e^2)^2}\left(5\cos(i)^2 - 1\right) - \frac{3}{2}J_2\left(\frac{R_\oplus}{a}\right)^2 \frac{1}{(1-e^2)^2}\cos(i)^2 +$$
$$+ 1 + \frac{3}{4}J_2\left(\frac{R_\oplus}{a}\right)^2 \frac{1}{(1-e^2)^2}\sqrt{1-e^2}\left(3\cos(i)^2 - 1\right)$$

$$g_{22} = \dot{\omega}_{22} + \dot{M}_{22} + \dot{\Omega}_{22}\cos(i) = \tag{A.16}$$
$$= 1 - \frac{\left(5\left(2 - e_x^2 - e_y^2\right)J_{22}R_\oplus^4\sin(i)\right)}{\left(64a^4\left(1 - e_x^2 - e_y^2\right)^{7/2}\right)} + \left(J_{22}R_\oplus^4\cos(i)^2\left(-\frac{45}{8}\right.\right.$$
$$+ \frac{3}{4}\left(e_x^2 + e_y^2\right) + \frac{9}{32}\left(e_x^2 + e_y^2\right)^2 + \left(\frac{57}{8} - \frac{69}{32}\left(e_x^2 + e_y^2\right) +\right.$$
$$\left.\left.+ \frac{27}{64}\left(e_x^2 + e_y^2\right)^2\right)\sin(i)^2\right)\Big) / \left(a^4\left(1 - e_x^2 - e_y^2\right)^4\right) +$$
$$+ \left(J_{22}R_\oplus^4\left(\frac{27}{2} - \frac{15}{16}\left(e_x^2 + e_y^2\right) - \frac{9}{16}\left(e_x^2 + e_y^2\right)^2 + \left(\frac{507}{16} +\right.\right.\right.$$
$$+ \frac{171}{32}\left(e_x^2 + e_y^2\right) + \frac{99}{64}\left(e_x^2 + e_y^2\right)^2\Big)\sin(i)^2 + \left(\frac{1185}{64} +\right.$$
$$\left.\left.\left.- \frac{675}{128}\left(e_x^2 + e_y^2\right) - \frac{135}{128}\left(e_x^2 + e_y^2\right)^2\right)\sin(i)^4\right)\right) / \left(a^4\left(1 - e_x^2 - e_y^2\right)^4\right)$$

Partial derivatives with respect to a

$$\frac{\partial\Omega}{\partial a} = \frac{3J_2R_\oplus^2\cos(i)}{a^3\left(1 - e_x^2 - e_y^2\right)^2} \tag{A.17}$$

$$\frac{\partial\omega}{\partial a} = -\frac{3J_2R_\oplus^2\left(-1 + 5\cos(i)^2\right)}{2a^3\left(1 - e_x^2 - e_y^2\right)^2} \tag{A.18}$$

$$\frac{\partial M}{\partial a} = -\frac{3J_2R_\oplus^2\left(-1 + 3\cos(i)^2\right)}{2a^3\left(1 - e_x^2 - e_y^2\right)^{3/2}} \tag{A.19}$$

$$\frac{\partial g}{\partial a} = \frac{3J_2R_\oplus^2\cos(i)^2}{a^3\left(1 - e_x^2 - e_y^2\right)^2} - \frac{3J_2R_\oplus^2\left(-1 + 3\cos(i)^2\right)}{2a^3\left(1 - e_x^2 - e_y^2\right)^{3/2}} - \frac{3J_2R_\oplus^2\left(-1 + 5\cos(i)^2\right)}{2a^3\left(1 - e_x^2 - e_y^2\right)^2} \tag{A.20}$$

$$\frac{\partial \Omega_{22}}{\partial a} = -\left(4J_{22}R_{\oplus}^{4}\cos(i)\left(-\frac{45}{8}+\frac{3}{4}\left(e_x^2+e_y^2\right)+\frac{9}{32}+\left(e_x^2+e_y^2\right)^2+\right.\right. \tag{A.21}$$
$$\left.\left.+\left(\frac{57}{8}-\frac{69}{32}\left(e_x^2+e_y^2\right)+\frac{27}{64}\left(e_x^2+e_y^2\right)^2\right)\sin(i)^2\right)\right)/\left(a^5\left(1-e_x^2-e_y^2\right)^4\right)$$

$$\frac{\partial \omega_{22}}{\partial a} = -\left(4J_{22}R_{\oplus}^{4}\left(\frac{27}{2}-\frac{15}{16}\left(e_x^2+e_y^2\right)-\frac{9}{16}\left(e_x^2+e_y^2\right)^2+\right.\right. \tag{A.22}$$
$$+\left(\frac{507}{16}+\frac{171}{32}\left(e_x^2+e_y^2\right)+\frac{99}{64}\left(e_x^2+e_y^2\right)^2\right)\sin(i)^2+\left(\frac{1185}{64}+\right.$$
$$\left.\left.-\frac{675}{128}\left(e_x^2+e_y^2\right)-\frac{135}{128}\left(e_x^2+e_y^2\right)^2\right)\sin(i)^4\right)\right)/\left(a^5\left(1-e_x^2-e_y^2\right)^4\right)$$

$$\frac{\partial M_{22}}{\partial a} = \left(5\left(2-e_x^2-e_y^2\right)J_{22}R_{\oplus}^{4}\sin(i)\right)/\left(16a^5\left(1-e_x^2-e_y^2\right)^{7/2}\right) \tag{A.23}$$

$$\frac{\partial g_{22}}{\partial a} = \left(5\left(2-e_x^2-e_y^2\right)J_{22}R_{\oplus}^{4}\sin(i)\right)/\left(16a^5\left(1-e_x^2-e_y^2\right)^{7/2}\right)+ \tag{A.24}$$
$$-\left(4J_{22}R_{\oplus}^{4}\cos(i)^2\left(-\frac{45}{8}+\frac{3}{4}\left(e_x^2+e_y^2\right)+\frac{9}{32}\left(e_x^2+e_y^2\right)^2+\left(\frac{57}{8}+\right.\right.\right.$$
$$\left.\left.\left.-\frac{69}{32}\left(e_x^2+e_y^2\right)+\frac{27}{64}\left(e_x^2+e_y^2\right)^2\right)\sin(i)^2\right)\right)/\left(a^5\left(1-e_x^2-e_y^2\right)^4\right)+$$
$$-\left(4J_{22}R_{\oplus}^{4}\left(\frac{27}{2}-\frac{15}{16}\left(e_x^2+e_y^2\right)-\frac{9}{16}\left(e_x^2+e_y^2\right)^2+\left(\frac{507}{16}+\right.\right.\right.$$
$$+\left.\frac{171}{32}\left(e_x^2+e_y^2\right)+\frac{99}{64}\left(e_x^2+e_y^2\right)^2\right)\sin(i)^2+\left(\frac{1185}{64}-\frac{675}{128}\left(e_x^2+e_y^2\right)+\right.$$
$$\left.\left.\left.-\frac{135}{128}\left(e_x^2+e_y^2\right)^2\right)\sin(i)^4\right)\right)/\left(a^5\left(1-e_x^2-e_y^2\right)^4\right)$$

Partial derivatives with respect to i

$$\frac{\partial \Omega}{\partial i} = \frac{3J_2R_{\oplus}^{2}\sin(i)}{2a^2\left(1-e_x^2-e_y^2\right)^2} \tag{A.25}$$

$$\frac{\partial \omega}{\partial i} = -\frac{15J_2R_{\oplus}^{2}\cos(i)\sin(i)}{2a^2\left(1-e_x^2-e_y^2\right)^2} \tag{A.26}$$

$$\frac{\partial M}{\partial i} = -\frac{9J_2R_{\oplus}^{2}\cos(i)\sin(i)}{2a^2\left(1-e_x^2-e_y^2\right)^{3/2}} \tag{A.27}$$

$$\frac{\partial g}{\partial i} = -\frac{9J_2R_\oplus^2\cos(i)\sin(i)}{2a^2\left(1-e_x^2-e_y^2\right)^2} - \frac{9J_2R_\oplus^2\cos(i)\sin(i)}{2a^2\left(1-e_x^2-e_y^2\right)^{3/2}} \tag{A.28}$$

$$\frac{\partial \Omega_{22}}{\partial i} = \frac{2\left(\frac{57}{8} - \frac{69}{32}\left(e_x^2+e_y^2\right) + \frac{27}{64}\left(e_x^2+e_y^2\right)^2\right)J_{22}R_\oplus^4\cos(i)^2\sin(i)}{a^4\left(1-e_x^2-e_y^2\right)^4} + \tag{A.29}$$
$$- \left(J_{22}R_\oplus^4\sin(i)\left(-\frac{45}{8} + \frac{3}{4}\left(e_x^2+e_y^2\right) + \frac{9}{32}\left(e_x^2+e_y^2\right)^2 + \left(\frac{57}{8} + \right.\right.\right.$$
$$\left.\left.\left. - \frac{69}{32}\left(e_x^2+e_y^2\right) + \frac{27}{64}\left(e_x^2+e_y^2\right)^2\right)\sin(i)^2\right)\right) / \left(a^4\left(1-e_x^2-e_y^2\right)^4\right)$$

$$\frac{\partial \omega_{22}}{\partial i} = \left(J_{22}R_\oplus^4\left(2\left(\frac{507}{16} + \frac{171}{32}\left(e_x^2+e_y^2\right) + \right.\right.\right. \tag{A.30}$$
$$\left. + \frac{99}{64}\left(e_x^2+e_y^2\right)^2\right)\cos(i)\sin(i) + 4\left(\frac{1185}{64} - \frac{675}{128}\left(e_x^2+e_y^2\right) + \right.$$
$$\left.\left.\left. - \frac{135}{128}\left(e_x^2+e_y^2\right)^2\right)\cos(i)\sin(i)^3\right)\right) / \left(a^4\left(1-e_x^2-e_y^2\right)^4\right)$$

$$\frac{\partial M_{22}}{\partial i} = -\frac{5\left(2-e_x^2-e_y^2\right)J_{22}R_\oplus^4\cos(i)}{64a^4\left(1-e_x^2-e_y^2\right)^{7/2}} \tag{A.31}$$

$$\frac{\partial g_{22}}{\partial i} = -\frac{5\left(2-e_x^2-e_y^2\right)J_{22}R_\oplus^4\cos(i)}{64a^4\left(1-e_x^2-e_y^2\right)^{7/2}} + \left(2\left(\frac{57}{8} - \frac{69}{32}\left(e_x^2+e_y^2\right) + \right.\right. \tag{A.32}$$
$$\left. + \frac{27}{64}\left(e_x^2+e_y^2\right)^2\right)J_{22}R_\oplus^4\cos(i)^3\sin(i)\right) / \left(a^4\left(1-e_x^2-e_y^2\right)^4\right) +$$
$$- \left(2J_{22}R_\oplus^4\cos(i)\sin(i)\left(-\frac{45}{8} + \frac{3}{4}\left(e_x^2+e_y^2\right) + \frac{9}{32}\left(e_x^2+e_y^2\right)^2 + \right.\right.$$
$$\left.\left. + \left(\frac{57}{8} - \frac{69}{32}\left(e_x^2+e_y^2\right) + \frac{27}{64}\left(e_x^2+e_y^2\right)^2\right)\sin(i)^2\right)\right) / \left(a^4\left(1-e_x^2-e_y^2\right)^4\right)$$
$$- \left(J_{22}R_\oplus^4\left(2\left(\frac{507}{16} + \frac{171}{32}\left(e_x^2+e_y^2\right) + \right.\right.\right.$$
$$\left. + \frac{99}{64}\left(e_x^2+e_y^2\right)^2\right)\cos(i)\sin(i) + 4\left(\frac{1185}{64} - \frac{675}{128}\left(e_x^2+e_y^2\right)\right.$$
$$\left.\left.\left. - \frac{135}{128}\left(e_x^2+e_y^2\right)^2\right)\cos(i)\sin(i)^3\right)\right) / \left(a^4\left(1-e_x^2-e_y^2\right)^4\right)$$

Partial derivatives with respect to e_x

$$\frac{\partial \Omega}{\partial e_x} = -\frac{6e_x J_2 R_\oplus^2 \cos(i)}{a^2\left(1-e_x^2-e_y^2\right)^3} \tag{A.33}$$

$$\frac{\partial \omega}{\partial e_x} = \frac{3e_x J_2 R_\oplus^2\left(-1+5\cos(i)^2\right)}{a^2\left(1-e_x^2-e_y^2\right)^3} \tag{A.34}$$

$$\frac{\partial M}{\partial e_x} = \frac{9e_x J_2 R_\oplus^2\left(-1+3\cos(i)^2\right)}{4a^2\left(1-e_x^2-e_y^2\right)^{5/2}} \tag{A.35}$$

$$\begin{aligned}\frac{\partial g}{\partial e_x} = &-\frac{6e_x J_2 R_\oplus^2\cos(i)^2}{a^2\left(1-e_x^2-e_y^2\right)^3} + \frac{9e_x J_2 R_\oplus^2\left(-1+3\cos(i)^2\right)}{4a^2\left(1-e_x^2-e_y^2\right)^{5/2}} + \\ &+ \frac{3e_x J_2 R_\oplus^2\left(-1+5\cos(i)^2\right)}{a^2\left(1-e_x^2-e_y^2\right)^3}\end{aligned} \tag{A.36}$$

$$\begin{aligned}\frac{\partial \Omega_{22}}{\partial e_x} = &\frac{J_{22}R_\oplus^4\cos i\left(\frac{3e_x}{2}+\frac{9}{8}e_x\left(e_x^2+e_y^2\right)-\left(\frac{69e_x}{16}-\frac{27}{16}e_x\left(e_x^2+e_y^2\right)\right)\sin i^2\right)}{a^4\left(1-e_x^2-e_y^2\right)^4} + \\ &+\left(8e_x J_{22}R_\oplus^4\cos(i)\left(-\frac{45}{8}+\frac{3}{4}\left(e_x^2+e_y^2\right)+\frac{9}{32}\left(e_x^2+e_y^2\right)^2+\right.\right. \\ &+\left.\left.\left(\frac{57}{8}-\frac{69}{32}\left(e_x^2+e_y^2\right)+\frac{27}{64}\left(e_x^2+e_y^2\right)^2\right)\sin(i)^2\right)\right)/\left(a^4\left(1-e_x^2-e_y^2\right)^5\right)\end{aligned} \tag{A.37}$$

$$\begin{aligned}\frac{\partial \omega_{22}}{\partial e_x} = &\left(J_{22}R_\oplus^4\left(-\frac{15e_x}{8}-\frac{9}{4}e_x\left(e_x^2+e_y^2\right)+\left(\frac{171e_x}{16}+\frac{99}{16}e_x\left(e_x^2+e_y^2\right)\right)\sin i^2+\right.\right. \\ &+\left.\left.\left(-\frac{675e_x}{64}-\frac{135}{32}e_x\left(e_x^2+e_y^2\right)\right)\sin(i)^4\right)\right)/\left(a^4\left(1-e_x^2-e_y^2\right)^4\right)+ \\ &+\left(8e_x J_{22}R_\oplus^4\left(\frac{27}{2}-\frac{15}{16}\left(e_x^2+e_y^2\right)-\frac{9}{16}\left(e_x^2+e_y^2\right)^2+\left(\frac{507}{16}+\right.\right.\right. \\ &+\left.\frac{171}{32}\left(e_x^2+e_y^2\right)+\frac{99}{64}\left(e_x^2+e_y^2\right)^2\right)\sin(i)^2+\left(\frac{1185}{64}-\frac{675}{128}\left(e_x^2+e_y^2\right)+\right. \\ &-\left.\left.\left.\frac{135}{128}\left(e_x^2+e_y^2\right)^2\right)\sin(i)^4\right)\right)/\left(a^4\left(1-e_x^2-e_y^2\right)^5\right)\end{aligned} \tag{A.38}$$

$$\frac{\partial M_{22}}{\partial e_x} = \frac{5e_x J_{22}R_\oplus^4\sin(i)}{32a^4\left(1-e_x^2-e_y^2\right)^{7/2}} - \frac{35e_x\left(2-e_x^2-e_y^2\right)J_{22}R_\oplus^4\sin(i)}{64a^4\left(1-e_x^2-e_y^2\right)^{9/2}} \tag{A.39}$$

$$\frac{\partial g_{22}}{\partial e_x} = \frac{5e_x J_{22} R_\oplus^4 \sin(i)}{32a^4\left(1-e_x^2-e_y^2\right)^{7/2}} - \frac{35e_x\left(2-e_x^2-e_y^2\right) J_{22} R_\oplus^4 \sin(i)}{64a^4\left(1-e_x^2-e_y^2\right)^{9/2}} + \tag{A.40}$$
$$+ \left(J_{22} R_\oplus^4 \cos(i)^2 \left(\frac{3e_x}{2} + \frac{9}{8}e_x\left(e_x^2+e_y^2\right) + \left(-\frac{69e_x}{16} + \right.\right.\right.$$
$$+ \left.\left.\left. \frac{27}{16}e_x\left(e_x^2+e_y^2\right)\right)\sin(i)^2\right)\right) / \left(a^4\left(1-e_x^2-e_y^2\right)^4\right) +$$
$$+ \left(8e_x J_{22} R_\oplus^4 \cos(i)^2 \left(-\frac{45}{8} + \frac{3}{4}\left(e_x^2+e_y^2\right) + \frac{9}{32}\left(e_x^2+e_y^2\right)^2 + \left(\frac{57}{8} + \right.\right.\right.$$
$$- \left.\left.\left. \frac{69}{32}\left(e_x^2+e_y^2\right) + \frac{27}{64}\left(e_x^2+e_y^2\right)^2\right)\sin(i)^2\right)\right) / \left(a^4\left(1-e_x^2-e_y^2\right)^5\right) +$$
$$+ \left(J_{22} R_\oplus^4 \left(-\frac{15e_x}{8} - \frac{9}{4}e_x\left(e_x^2+e_y^2\right) + \left(\frac{171e_x}{16} + \frac{99}{16}e_x\left(e_x^2+e_y^2\right)\right)\sin(i)^2\right.\right.$$
$$+ \left.\left. \left(-\frac{675e_x}{64} - \frac{135}{32}e_x\left(e_x^2+e_y^2\right)\right)\sin(i)^4\right)\right) / \left(a^4\left(1-e_x^2-e_y^2\right)^4\right) +$$
$$+ \left(8e_x J_{22} R_\oplus^4 \left(\frac{27}{2} - \frac{15}{16}\left(e_x^2+e_y^2\right) - \frac{9}{16}\left(e_x^2+e_y^2\right)^2 + \left(\frac{507}{16} + \right.\right.\right.$$
$$+ \left.\left.\left. \frac{171}{32}\left(e_x^2+e_y^2\right) + \frac{99}{64}\left(e_x^2+e_y^2\right)^2\right)\sin(i)^2 + \left(\frac{1185}{64} - \frac{675}{128}\left(e_x^2+e_y^2\right) + \right.\right.\right.$$
$$- \left.\left.\left. \frac{135}{128}\left(e_x^2+e_y^2\right)^2\right)\sin(i)^4\right)\right) / \left(a^4\left(1-e_x^2-e_y^2\right)^5\right)$$

Partial derivatives with respect to e_y

$$\frac{\partial \Omega}{\partial e_y} = -\frac{6e_y J_2 R_\oplus^2 \cos(i)}{a^2\left(1-e_x^2-e_y^2\right)^3} \tag{A.41}$$

$$\frac{\partial \omega}{\partial e_y} = \frac{3e_y J_2 R_\oplus^2\left(-1+5\cos(i)^2\right)}{a^2\left(1-e_x^2-e_y^2\right)^3} \tag{A.42}$$

$$\frac{\partial M}{\partial e_y} = \frac{9e_y J_2 R_\oplus^2\left(-1+3\cos(i)^2\right)}{4a^2\left(1-e_x^2-e_y^2\right)^{5/2}} \tag{A.43}$$

$$\frac{\partial g}{\partial e_y} = -\frac{6e_y J_2 R_\oplus^2 \cos(i)^2}{a^2\left(1-e_x^2-e_y^2\right)^3} + \frac{9e_y J_2 R_\oplus^2\left(-1+3\cos(i)^2\right)}{4a^2\left(1-e_x^2-e_y^2\right)^{5/2}} + \tag{A.44}$$
$$+ \frac{3e_y J_2 R_\oplus^2\left(-1+5\cos(i)^2\right)}{a^2\left(1-e_x^2-e_y^2\right)^3}$$

$$\frac{\partial \Omega_{22}}{\partial e_y} = \frac{J_{22}R_{\oplus}^4 \cos i \left(\frac{3e_y}{2} + \frac{9}{8}e_y \left(e_x^2 + e_y^2\right) - \left(\frac{69e_y}{16} - \frac{27}{16}e_y \left(e_x^2 + e_y^2\right) \right) \sin i^2 \right)}{a^4 \left(1 - e_x^2 - e_y^2\right)^4} + \tag{A.45}$$
$$+ \left(8e_y J_{22} R_{\oplus}^4 \cos(i) \left(-\frac{45}{8} + \frac{3}{4}\left(e_x^2 + e_y^2\right) + \frac{9}{32}\left(e_x^2 + e_y^2\right)^2 + \right.\right.$$
$$\left.\left. + \left(\frac{57}{8} - \frac{69}{32}\left(e_x^2 + e_y^2\right) + \frac{27}{64}\left(e_x^2 + e_y^2\right)^2 \right) \sin(i)^2 \right) \right) / \left(a^4 \left(1 - e_x^2 - e_y^2\right)^5 \right)$$

$$\frac{\partial \omega_{22}}{\partial e_y} = \left(J_{22}R_{\oplus}^4 \left(-\frac{15e_y}{8} - \frac{9}{4}e_y \left(e_x^2 + e_y^2\right) + \left(\frac{171e_y}{16} + \frac{99}{16}e_y \left(e_x^2 + e_y^2\right) \right) \sin i^2 + \right.\right. \tag{A.46}$$
$$\left.\left. + \left(-\frac{675e_y}{64} - \frac{135}{32}e_y \left(e_x^2 + e_y^2\right) \right) \sin(i)^4 \right) \right) / \left(a^4 \left(1 - e_x^2 - e_y^2\right)^4 \right) +$$
$$+ \left(8e_y J_{22} R_{\oplus}^4 \left(\frac{27}{2} - \frac{15}{16}\left(e_x^2 + e_y^2\right) - \frac{9}{16}\left(e_x^2 + e_y^2\right)^2 + \left(\frac{507}{16} + \right.\right.\right.$$
$$\left.\left.\left. + \frac{171}{32}\left(e_x^2 + e_y^2\right) + \frac{99}{64}\left(e_x^2 + e_y^2\right)^2 \right) \sin(i)^2 + \left(\frac{1185}{64} - \frac{675}{128}\left(e_x^2 + e_y^2\right) + \right.\right.\right.$$
$$\left.\left.\left. - \frac{135}{128}\left(e_x^2 + e_y^2\right)^2 \right) \sin(i)^4 \right) \right) / \left(a^4 \left(1 - e_x^2 - e_y^2\right)^5 \right)$$

$$\frac{\partial M_{22}}{\partial e_y} = \frac{5e_y J_{22} R_{\oplus}^4 \sin(i)}{32a^4 \left(1 - e_x^2 - e_y^2\right)^{7/2}} - \frac{35e_y \left(2 - e_x^2 - e_y^2\right) J_{22} R_{\oplus}^4 \sin(i)}{64a^4 \left(1 - e_x^2 - e_y^2\right)^{9/2}} \tag{A.47}$$

$$\frac{\partial g_{22}}{\partial e_y} = \frac{5e_y J_{22} R_\oplus^4 \sin(i)}{32a^4\left(1-e_x^2-e_y^2\right)^{7/2}} - \frac{35e_y\left(2-e_x^2-e_y^2\right) J_{22} R_\oplus^4 \sin(i)}{64a^4\left(1-e_x^2-e_y^2\right)^{9/2}} + \tag{A.48}$$
$$+ \left(J_{22} R_\oplus^4 \cos(i)^2 \left(\frac{3e_y}{2} + \frac{9}{8}e_y\left(e_x^2+e_y^2\right) + \left(-\frac{69e_y}{16} + \right.\right.\right.$$
$$+ \left.\left.\left. \frac{27}{16}e_y\left(e_x^2+e_y^2\right)\right)\sin(i)^2\right)\right) / \left(a^4\left(1-e_x^2-e_y^2\right)^4\right) +$$
$$+ \left(8e_y J_{22} R_\oplus^4 \cos(i)^2 \left(-\frac{45}{8} + \frac{3}{4}\left(e_x^2+e_y^2\right) + \frac{9}{32}\left(e_x^2+e_y^2\right)^2 + \left(\frac{57}{8} + \right.\right.\right.$$
$$- \left.\left.\left. \frac{69}{32}\left(e_x^2+e_y^2\right) + \frac{27}{64}\left(e_x^2+e_y^2\right)^2\right)\sin(i)^2\right)\right) / \left(a^4\left(1-e_x^2-e_y^2\right)^5\right) +$$
$$+ \left(J_{22} R_\oplus^4 \left(-\frac{15e_y}{8} - \frac{9}{4}e_y\left(e_x^2+e_y^2\right) + \left(\frac{171e_y}{16} + \frac{99}{16}e_y\left(e_x^2+e_y^2\right)\right)\sin(i)^2\right.\right.$$
$$+ \left.\left. \left(-\frac{675e_y}{64} - \frac{135}{32}e_y\left(e_x^2+e_y^2\right)\right)\sin(i)^4\right)\right) / \left(a^4\left(1-e_x^2-e_y^2\right)^4\right) +$$
$$+ \left(8e_y J_{22} R_\oplus^4 \left(\frac{27}{2} - \frac{15}{16}\left(e_x^2+e_y^2\right) - \frac{9}{16}\left(e_x^2+e_y^2\right)^2 + \left(\frac{507}{16} + \right.\right.\right.$$
$$+ \left.\left.\left. \frac{171}{32}\left(e_x^2+e_y^2\right) + \frac{99}{64}\left(e_x^2+e_y^2\right)^2\right)\sin(i)^2 + \left(\frac{1185}{64} - \frac{675}{128}\left(e_x^2+e_y^2\right) + \right.\right.\right.$$
$$- \left.\left.\left. \frac{135}{128}\left(e_x^2+e_y^2\right)^2\right)\sin(i)^4\right)\right) / \left(a^4\left(1-e_x^2-e_y^2\right)^5\right)$$

Acknowledgements

The LaTeXtemplate states: "Here you might want to acknowledge someone..". I think that it "might" be right. Without these "someones", this section would not even exist.

First of all, I want to thank Professor Camilla Colombo. Her passion for teaching Orbital Mechanics and Her humanity have made that She was the first option as a supervisor when I thought about my Master Thesis. Since the first meeting, the constant support has guided me up to these last days and, even in difficult times, Her presence has never been missed. Among all the numerous specialisations Professor Colombo is involved in, Formation Flying had me. Being part of Her research team has been a privilege and an honour. The obtained results were possible only by embracing Her work ethic and organization.

In this regard, I would like to also acknowledge my Co-Advisor Doctor Francesca Scala. I am extremely grateful to Francesca for overseeing this work from start to finish. Her help and sharp insights have been immensely constructive, especially during the practical implementation of this Thesis. I chose this field mainly driven by curiosity and confidence that Relative Motion will be constantly more important in the space industry. Although, if I had known that Francesca would have been my Co-Advisor, I would have selected it a priori.

My gratitude also goes to Politecnico di Milano. Five years have passed since my first lecture in Bovisa and I still remember the excitement. A new beginning is now in on sight and if I am itching to embrace it, it is only because of all I have learned, the wonderful people I have met and the moments experienced between those desks.

Finally, a huge thanks to all those that have succeeded in bearing me for all this time.

Bibliography

[1] Andrew Hansen, Karen Van Dyke, Calvin Miles, and John W. Lavrakas. Gps civil signal monitoring - advancing toward implementation. *27th International Technical Meeting of the Satellite Division of the Institute of Navigation, ION GNSS 2014*, 4, 2014.

[2] Jesse Leitner. Formation flying – the future of remote sensing from space. *18th International Symposium on Space Flight Dynamics*, 2004.

[3] GNSS Science Support Centre. *Satellite Formation Flying - Navipedia*, 2018. URL `https://gssc.esa.int/navipedia/index.php/Satellite_Formation_Flying`.

[4] Jonathan P. Gardner, John C. Mather, Mark Clampin, Rene Doyon, Matthew A. Greenhouse, Heidi B. Hammel, John B. Hutchings, Peter Jakobsen, Simon J. Lilly, Knox S. Long, Jonathan I. Lunine, Mark J. Mccaughrean, Matt Mountain, John Nella, George H. Rieke, Marcia J. Rieke, Hans-Walter Rix, Eric P. Smith, George Sonneborn, Massimo Stiavelli, H. S. Stockman, Rogier A. Windhorst, and Gillian S. Wright. The james webb space telescope. *Space Science Reviews*, 123:485–606, 4 2006. ISSN 0038-6308. doi: 10.1007/s11214-006-8315-7. URL `https://link.springer.com/10.1007/s11214-006-8315-7`.

[5] Teri Grimwood. *UCS Satellite Database*, 2022. URL `www.ucsusa.org/resources/satellite-database`.

[6] R.E. Denton, B.U.O. Sonnerup, H. Hasegawa, T. D. Phan, C.T. Russell, R.J. Strangeway, B.L. Giles, D. Gershman, and R.B. Torbert. Motion of the mms spacecraft relative to the magnetic reconnection structure observed on 16 october 2015 at 1307 ut. *Geophysical Research Letters*, 43:5589–5596, 6 2016. ISSN 00948276. doi: 10.1002/2016GL069214. URL `http://doi.wiley.com/10.1002/2016GL069214`.

[7] DeLee Smith. *MMS: Studying the Explosive Magnetic Environment Around Earth | NASA*, 2021. URL `https://www.nasa.gov/mission_pages/mms/overview/index.html`.

[8] Markus Landgraf and Agnes Mestreau-Garreau. Formation flying and mission design

for proba-3. *Acta Astronautica*, 82:137–145, 1 2013. ISSN 00945765. doi: 10.1016/j.actaastro.2012.03.028. URL https://linkinghub.elsevier.com/retrieve/pii/S0094576512001002.

[9] Alex Cropp. *ESA - Proba-3: set the controls for the verge of the Sun*, 2016. URL https://www.esa.int/Enabling_Support/Space_Engineering_Technology/Proba_Missions/Proba-3_set_the_controls_for_the_verge_of_the_Sun.

[10] Laura Plice, Andres Dono Perez, and Stephen West. Helioswarm: Swarm mission design in high altitude orbit for heliophysics. *Advances in the Astronautical Sciences*, 171, 2020. ISSN 00653438.

[11] Jeff Foust. *NASA selects two heliophysics missions - SpaceNews*, 2022. URL https://spacenews.com/nasa-selects-two-heliophysics-missions/.

[12] Zhen Yang, Ya-Zhong Luo, and Jin Zhang. Second-order analytical solution of relative motion in j2-perturbed elliptic orbits. *Journal of Guidance, Control, and Dynamics*, 41:2258–2270, 10 2018. ISSN 0731-5090. doi: 10.2514/1.G003573. URL https://arc.aiaa.org/doi/10.2514/1.G003573.

[13] Marco Sabatini and Giovanni B. Palmerini. Linearized formation-flying dynamics in a perturbed orbital environment. *2008 IEEE Aerospace Conference*, pages 1–13, 3 2008. ISSN 1095-323X. doi: 10.1109/AERO.2008.4526271. URL http://ieeexplore.ieee.org/document/4526271/.

[14] Gabriella Gaias, Jean-Sébastien Ardaens, and Oliver Montenbruck. Model of

$$j_2$$

j 2 perturbed satellite relative motion with time-varying differential drag. *Celestial Mechanics and Dynamical Astronomy*, 123:411–433, 12 2015. ISSN 0923-2958. doi: 10.1007/s10569-015-9643-2. URL http://link.springer.com/10.1007/s10569-015-9643-2.

[15] Y.H. Kerr, P. Waldteufel, J.-P. Wigneron, J. Martinuzzi, J. Font, and M. Berger. Soil moisture retrieval from space: the soil moisture and ocean salinity (smos) mission. *IEEE Transactions on Geoscience and Remote Sensing*, 39:1729–1735, 2001. ISSN 01962892. doi: 10.1109/36.942551. URL http://ieeexplore.ieee.org/document/942551/.

[16] Jacob Christensen, Anders Carlström, Anders Emrich, and Peter de Maagt. The geostationary atmospheric sounder (gas). In Roland Meynart, Steven P. Neeck, and

Haruhisa Shimoda, editors, *Sensors, Systems, and Next-Generation Satellites X*, volume 6361, page 636109, 9 2006. doi: 10.1117/12.689577. URL `http://proceedings.spiedigitallibrary.org/proceeding.aspx?doi=10.1117/12.689577`.

[17] Cheng Zhang, Hao Liu, Ji Wu, Shengwei Zhang, Jingye Yan, Lijie Niu, Weiying Sun, and Huiling Li. Imaging analysis and first results of the geostationary interferometric microwave sounder demonstrator. *IEEE Transactions on Geoscience and Remote Sensing*, 53:207–218, 1 2015. ISSN 0196-2892. doi: 10.1109/TGRS.2014.2320983. URL `http://ieeexplore.ieee.org/document/6815741/`.

[18] Anders Carlstrom, Jacob Christensen, Johan Embretsen, Anders Emrich, and Peter de Maagt. A geostationary atmospheric sounder for now-casting and short-range weather forecasting. In *2009 IEEE Antennas and Propagation Society International Symposium*, pages 1–4. IEEE, 6 2009. ISBN 978-1-4244-3647-7. doi: 10.1109/APS.2009.5172067. URL `http://ieeexplore.ieee.org/document/5172067/`.

[19] Xi Guo, Hao Liu, Lijie Niu, Cheng Zhang, Hao Lu, Changxing Huo, Te Wang, and Ji Wu. Data processing and experimental performance of gims-ii (geostationary interferometric microwave sounder-second generation) demonstrator. *2018 IEEE 15th Specialist Meeting on Microwave Radiometry and Remote Sensing of the Environment (MicroRad)*, pages 1–4, 3 2018. doi: 10.1109/MICRORAD.2018.8430718. URL `https://ieeexplore.ieee.org/document/8430718/`.

[20] Andrea Monti Guarnieri and Stefano Tebaldini. On the exploitation of target statistics for sar interferometry applications. *IEEE Transactions on Geoscience and Remote Sensing*, 46:3436–3443, 11 2008. ISSN 0196-2892. doi: 10.1109/TGRS.2008.2001756. URL `http://ieeexplore.ieee.org/document/4685949/`.

[21] Ahmed Kiyoshi Sugihara and El Maghraby. *Microwave Interferometric Radiometry with Satellite Formation Flight for Earth Observation.* PhD thesis, University of Southampton, 2019. by Thesis for the degree of Doctor of Philosophy. Supervisors: Dr. Angelo Grubisic and Dr. Camilla Cogo. Examiners: Manuel Martin Neira and Alexander Wittig.

[22] Richard H. Vassar and Richard B. Sherwood. Formationkeeping for a pair of satellites in a circular orbit. *Journal of Guidance, Control, and Dynamics*, 8:235–242, 3 1985. ISSN 0731-5090. doi: 10.2514/3.19965. URL `https://arc.aiaa.org/doi/10.2514/3.19965`.

[23] Yuri Ulybyshev. Long-term formation keeping of satellite constellation using linear-quadratic controller. *Journal of Guidance, Control, and Dynamics*, 21:109–115, 1

1998. ISSN 0731-5090. doi: 10.2514/2.4204. URL https://arc.aiaa.org/doi/10.2514/2.4204.

[24] S.R. Starin, R.K. Yedavalli, and A.G. Sparks. Design of a lqr controller of reduced inputs for multiple spacecraft formation flying. *Proceedings of the 2001 American Control Conference. (Cat. No.01CH37148)*, 2:1327–1332 vol.2, 2001. ISSN 07431619. doi: 10.1109/ACC.2001.945908. URL http://ieeexplore.ieee.org/document/945908/.

[25] F. Y. Hadaegh, A. R. Ghavimi, G. Singh, and M Quadrelli. A centralized optimal controller for formation flying spacecraft. *International Conference on Intelligent Technologies*, pages 1–6, 9 2000. URL http://hdl.handle.net/2014/16143.

[26] Francesca Scala, Gabriella Gaias, Camilla Colombo, and Manuel Martin-Neira. Three satellites formation flying: Deployment and formation acquisition using relative orbital elements. *2020 AAS/AIAA Astrodynamics Specialist Conference*, 2020.

[27] Simone D'Amico and Oliver Montenbruck. Proximity operations of formation-flying spacecraft using an eccentricity/inclination vector separation. *Journal of Guidance, Control, and Dynamics*, 29:554–563, 5 2006. ISSN 0731-5090. doi: 10.2514/1.15114. URL https://arc.aiaa.org/doi/10.2514/1.15114.

[28] K. Anflo and R. Möllerberg. Flight demonstration of new thruster and green propellant technology on the prisma satellite. *Acta Astronautica*, 65:1238–1249, 11 2009. ISSN 00945765. doi: 10.1016/j.actaastro.2009.03.056. URL https://linkinghub.elsevier.com/retrieve/pii/S0094576509001970.

[29] Adam W. Koenig, Tommaso Guffanti, and Simone D'Amico. New state transition matrices for spacecraft relative motion in perturbed orbits. *Journal of Guidance, Control, and Dynamics*, 40:1749–1768, 7 2017. ISSN 0731-5090. doi: 10.2514/1.G002409. URL https://arc.aiaa.org/doi/10.2514/1.G002409.

[30] David A. Vallado. *Orbital Mechanics Fundamentals*. John Wiley and Sons, Ltd, 12 2010. doi: 10.1002/9780470686652.eae285. URL https://onlinelibrary.wiley.com/doi/10.1002/9780470686652.eae285.

[31] G. W. Hill. Researches in the lunar theory. *American Journal of Mathematics*, 1: 5, 1878. ISSN 00029327. doi: 10.2307/2369430. URL https://www.jstor.org/stable/2369430?origin=crossref.

[32] S D'amico. Relative orbital elements as integration constants of hill's equations. Tech-

nical report, German Aerospace Center (Deutsches Zentrum fur Luft- und Raumfahrt DLR)-German Space Operations Center„ 2005.

[33] P. Micheau. *Spaceflight Dynamics*. Cepadues-Editions, 1995. Ed. by Jean-Pierre Carrou.

[34] Gabriella Gaias, Camilla Colombo, and Martin Lara. Analytical framework for precise relative motion in low earth orbits. *Journal of Guidance, Control, and Dynamics*, 43:915–927, 5 2020. ISSN 1533-3884. doi: 10.2514/1.G004716. URL https://arc.aiaa.org/doi/10.2514/1.G004716.

[35] Lawrence F Shampine and Mark W Reichelt. The matlab ode suite. *Society for Industrial and Applied Mathematics*, 18, 1997.

[36] W. M. Kaula. *Satellite orbit analyses for geodetic purposes*. Springer Berlin Heidelberg, 1963. doi: 10.1007/978-3-642-48130-7_19. URL http://link.springer.com/10.1007/978-3-642-48130-7_19.

[37] Richard H. Battin. *An Introduction to the Mathematics and Methods of Astrodynamics, Revised Edition*. American Institute of Aeronautics and Astronautics, 1 1999. ISBN 978-1-56347-342-5. doi: 10.2514/4.861543. URL https://arc.aiaa.org/doi/book/10.2514/4.861543.

[38] Howard Curtis. *Orbital Mechanics for Engineering Students*. Elsevier, 2010. ISBN 9780123747785. doi: 10.1016/C2009-0-19374-1. URL https://linkinghub.elsevier.com/retrieve/pii/C20090193741.

[39] Martin Lara. Improving efficiency of analytic orbit propagation under geopotential effects. *72 th International Astronautical Congress (IAC)*, pages 25–29, 2021.

[40] Simone D'Amico. *Autonomous Formation Flying in Low Earth Orbit*. PhD thesis, Delft University of Technology, 2010. Ph.D. Thesis.

[41] Michelle Chernick and Simone D'Amico. New closed-form solutions for optimal impulsive control of spacecraft relative motion. In *AIAA/AAS Astrodynamics Specialist Conference*. American Institute of Aeronautics and Astronautics, 9 2016. ISBN 978-1-62410-445-9. doi: 10.2514/6.2016-5659. URL https://arc.aiaa.org/doi/10.2514/6.2016-5659.

[42] Alejandro Montero Miñán. Continuous-time control of multiple-satellite formations using mean relative orbital elements. Master's thesis, Politecnico di Milano, 4 2021. Supervisor: Colombo, C. Space Engineering Master Thesis.

[43] Pilar Romero and Jose M. Gambi. Optimal control in the east/west station-keeping manoeuvres for geostationary satellites. *Aerospace Science and Technology*, 8:729–734, 12 2004. ISSN 12709638. doi: 10.1016/j.ast.2004.08.004. URL https://linkinghub.elsevier.com/retrieve/pii/S1270963804000987.

[44] Frank L. Lewis, Draguna L. Vrabie, and Vassilis L. Syrmos. *Optimal Control*. John Wiley and Sons, Inc., 1 2012. ISBN 9781118122631. doi: 10.1002/9781118122631. URL http://doi.wiley.com/10.1002/9781118122631.

[45] Matteo Paolo Clemente. Optimal control of low-thrust satellite formation-flying reconfiguration using a lqr considering collision avoidance and fuel balancing issues. Master's thesis, Politecnico di Torino, 2020. Supervisor: Battipede, M. Aerospace Engineering Master Thesis.

[46] Matthew Willis and Simone D'Amico. Analytical approach to spacecraft formation-flying with low-thrust relative spiral trajectories. *Acta Astronautica*, 153:175–190, 12 2018. ISSN 00945765. doi: 10.1016/j.actaastro.2018.02.002. URL https://linkinghub.elsevier.com/retrieve/pii/S0094576517313954.

[47] Gabriella Gaias and Marco Lovera. Trajectory design for proximity operations: The relative orbital elements' perspective. *Journal of Guidance, Control, and Dynamics*, 44:2294–2302, 12 2021. ISSN 1533-3884. doi: 10.2514/1.G006175. URL https://arc.aiaa.org/doi/10.2514/1.G006175.

[48] Hugo Nguyen, Johan Köhler, Lars Stenmark, and Uppsala University. The merits of cold gas micropropulsion in state-of-the-art space missions. *53rd International Astronautical Conference*, 2002.

[49] Vladimir Hruby, Manuel Gamero-Castaño, Paul Falkos, and Suren Shenoy. Micro newton colloid thruster system development. *Proc. 27th Int. Electric Propulsion Conf.*, 2001.

[50] Moriba Jah, Steven Hughes, Matthew Wilkins, and Tom Kelecy. The general mission analysis tool (gmat): A new resource for supporting debris orbit determination, tracking and analysis. *European Space Agency, (Special Publication) ESA SP*, 672 SP, 2009. ISSN 03796566.